SYNTHESIS AND BIOMEDICAL APPLICATIONS OF POLYMER NANOMATERIALS

By

TONG LIU

Bachelor of Science in Environmental Engineering

China University of Mining and Technology (Beijing)

Beijing, China

2009

Submitted to the Faculty of the
Graduate College of the
Oklahoma State University
in partial fulfillment of
the requirements for
the Degree of
MASTER OF SCIENCE
May, 2012

SYNTHESIS AND BIOMEDICAL APPLICATIONS OF

POLYMER NANOMATERIALS

Thesis Approved:

Dr. Yu Mao

Thesis Adviser

Dr. Hasan Atiyeh

Dr. Mark Wilkins

Dr. Sheryl A. Tucker

Dean of the Graduate College

TABLE OF CONTENTS

Chapter Page

LIST OF TABLES

Table Page

LIST OF FIGURES

Figure Page

Figure Page

CHAPTER I

INTRODUCTION

1.1 Polymeric biomaterials

A considerable endeavor has been taken on the development of biomaterials for biomedical applications in recent years. The term “biomaterials” normally refers to materials intended to interact with biological systems for therapeutic or diagnostic purposes [1, 2]. Biomaterials can be synthetic or natural materials. Synthetic polymers have been widely used in biomedical applications and expanded into new fields of biological engineering.

The use of synthetic polymers in biomedical applications can be tracked back to the beginning of polymer science. Almost every early synthetic polymer has been explored in surgical or therapeutic applications. In the early 1940s, nylon was used as a suture followed by poly(methyl methacrylate) (PMMA), polyvinyl chloride (PVC), Dacron polyester and other polymers in surgical uses [3]. In the 1950s, Drahoslaw and Wichterle proposed and synthesized a new biomaterial by copolymerizing 2-hydroxyethyl methacrylate (HEMA) with ethylene dimethacrylate (EDMA) for applications in ophthalmology [4]. Otto Wichterle developed the first polymer-based contact lenses via a spin casting process [5, 6]. In the meantime, the study of biocompatibility of polymeric materials began to attract researchers’ attention [7-9]. Polymer materials were further modified to expand their applications in biomedical engineering [7-9].

In this thesis, monomers of methacrylic acid (MAA) and 2-dimethylamino ethyl methacrylate (DMAEMA) were used to synthesize polymer nanomaterials for study in biomedical applications. MAA has been used to synthesize biomaterials with other monomers to enhance biocompatibility of polymers [10]. In addition, its stimuli-

responsive property has aroused great interest as well, which could be applied to drug/protein delivery [11-13]. DMAEMA containing polymers are also widely used in biomedical engineering because of their antibacterial and stimuli-responsive bioactive properties [14]. These polymers can be used as biocidal surfaces in medical devices and tissue engineering [14-19]. Since polymers containing DMAEMA have stimuli-responsive properties, they have been studied and applied to areas of tissue engineering, drug delivery and biosensor [14, 20, 21].

1.2 Polymers for antifouling surfaces

In clinical applications, implanted devices prevent self-healing and cause inflammation [22]. The use of implanted biomedical devices is limited because of poor control of immunological responses. Surface modification of devices is one acceptable way to suppress the foreign body reaction and promote wound healing [23]. For long-term uses, biomaterials need to be engineered to help the body regenerate new tissue and start self-healing process.

Figure 1.1 illustrates bacteria adherence and accumulation on an implanted material. Accumulation of bacteria and proteins can lead to inflammation and failure of implants. Surface modification with nonfouling coating can inhibit this foreign body reaction and allow the implanted devices to function normally.

Nonfouling materials have been studied since the 1960s. Merrill and co-workers intended to identify anti-thrombogenic materials and examined hydrophilic and hydrophobic polymers in detail [24-27]. They discovered that poly(ethylene glycol) (PEG)

could be an excellent antifouling biomaterial by resisting protein adsorption [28]. Since then, PEG has been widely used to create antifouling surfaces [29]. For long-term applications, however, degradation and loss of antifouling properties are caused by oxidation damage and enzymatic cleavage of PEG chains.

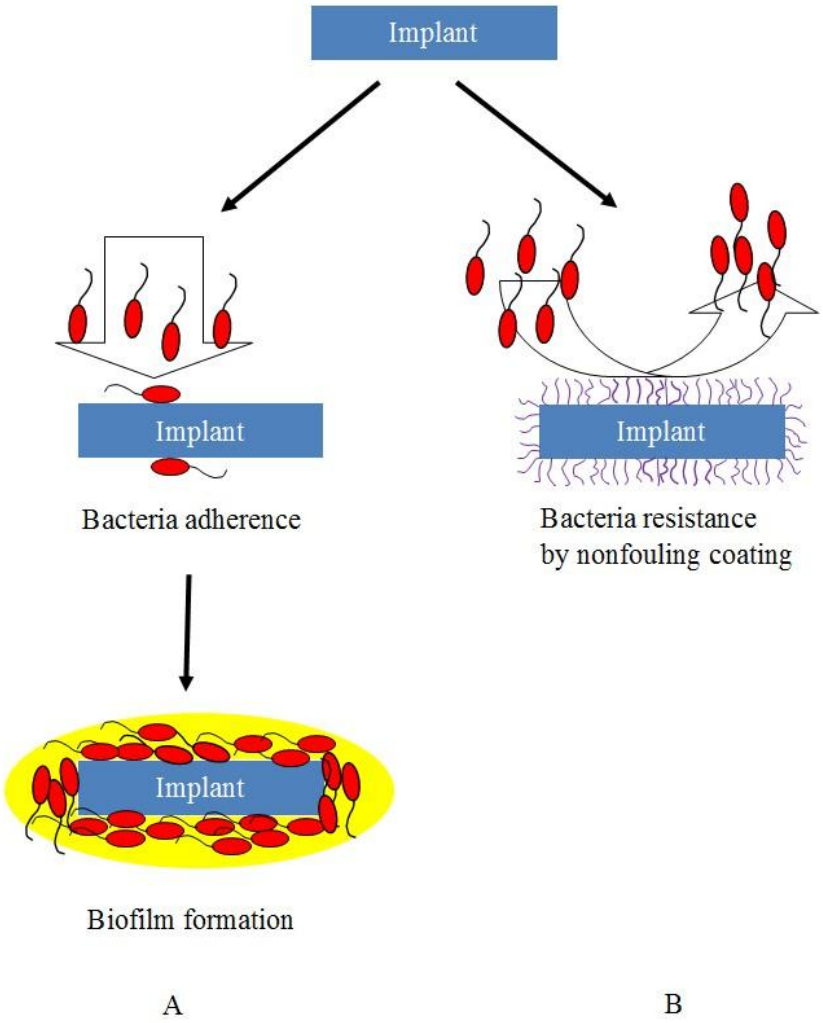

Figure 1.1 Bacteria accumulation on implanted devices (A) and bacteria resistance after surface modification with nonfouling coating (B).

To design a nonfouling surface, both chemical and structural properties need to be considered, including electrical neutrality and hydrophilicity [30, 31]. Zwitterionic

polymers and homogenously arranged polyampholytes have been considerably investigated as potential nonfouling materials [32, 33]. Jiang's group developed zwitterionic poly(sulfobetaine methacrylate) (PSBMA) and poly(carboxylbetaine methacrylate) (PCBMA) brushes to resist non-specific protein adsorption and bacteria accumulation [34, 35]. Although these zwitterionic polymers demonstrated excellent nonfouling ability, zwitterionic PCBMA polymer became partially protonated at low pH, which in turn compensated the electrostatic neutrality and resulted in protein adsorption [36].

1.3 Polymers for bone tissue engineering

For tissue regeneration, one of the best approaches is to replace the damaged tissue with materials that have similar chemical composition and micro-structure as three dimensional (3D) extracellular matrixes (ECM). To design scaffolds for bone tissue engineering, it is essential to understand the hierarchical structure of natural bone, which was studied by Weiner [37]. Figure 1.2 illustrates the hierarchical structure of bone composed of mineralized nanofibrils, which is the lowest level of the bone structure.

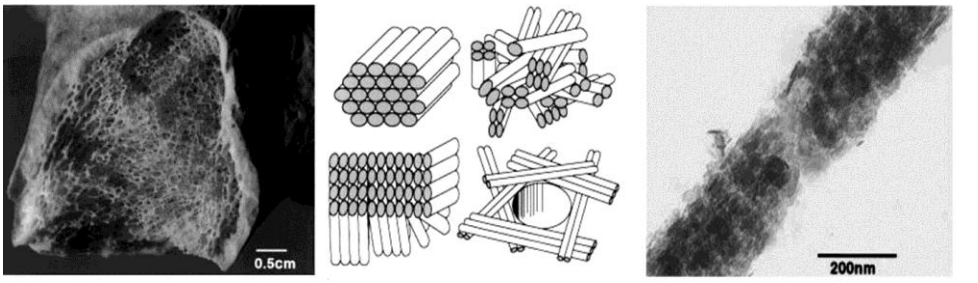

Figure 1.2 The hierarchical levels of bone structure [37].

Polymeric materials have been considered as excellent substrates for mineralization. They are capable of inducing the nuclei of apatite due to the functional groups, such as –COOH, -OH, and HPO_4, which play a similar role as surface functional groups in collagens [38]. Considerable research has been conducted on mineralization of fibrils and fabrication of 3D scaffolds [39, 40]. Self-assembled peptide-amphiphile nanofibers were synthesized and mineralized. The polymer nanofibers were able to promote oriented crystals [41]. Similarly, surface modified ethylene-vinyl alcohol copolymer (EVOH) fibers were investigated, and apatite deposited EVOH fibers were obtained [42]. Besides the two-dimensional fibers, 3D scaffolds were fabricated to obtain mineralized scaffolds, such as poly(ε-caprolactone) (PCL) fibrous structure [43], mineral content electrospun scaffolds [44], and porous polymer/ceramic composite scaffolds [45]. However, both the array structure of fibrils and the orientation of hydroxyapatite are two keys to activate the regenerative process [46]. Neither synthetic polymer fibers nor the reported mineralized scaffolds are an effective matrix for bone regeneration. The fabrication of 3D structural scaffolds with the capability of promoting oriented growth of apatite still needs further investigation.

1.4 Initiated chemical vapor deposition (iCVD)

Initiated chemical vapor deposition (iCVD) is a vapor based free radical polymerization process. Prior to reaction, monomers and initiator are vaporized. The gases are then delivered into a reactor. Initiator is decomposed by temperature around 250 ℃ into radicals and subsequently reacts with monomers to produce oligomers. As the molecules grow, they deposit onto substrates and generate free radical sites.

Polymerization propagation then takes place on the substrates to form polymer coatings. The technique allows polymerization and surface modification to be completed in a single step [47]. The solid polymer films have uniform thickness, and it is possible to control the thickness during the iCVD process [48]. In addition, iCVD can be utilized on materials regardless of the morphology and dimension of the surface [49]. Thus, nanoscale structure can be fabricated using iCVD.

1.5 Scope of thesis

Chapters II through IV are structured as journal articles, and therefore each chapter can be read as an independent research article. Each chapter contains sections including abstract, introduction, experimental, results, discussion and conclusion sections. Thus, the introduction of this thesis is intended to provide the general background and information.

Chapter II reports novel polyampholytes of poly(methacrylic acid-*co*-2-dimethylamino ethyl methacrylate-*co*-ethylene glycol diacrylate) synthesized via iCVD. These polyampholytes were subjected to bacteria adhesion and accumulation tests to examine their nonfouling capabilities.

Chapter III reports the antimicrobial effects of positively charged surfaces fabricated by iCVD. Copolymers of poly(2-dimethylamino ethyl methacrylate-*co*-ethylene glycol diacrylate) with different chemical compositions were subjected to bacteria adhesion and biofilm formation tests to investigate the effect of positive charges on antimicrobial effects.

Chapter IV presents the fabrication of aligned polymeric nanotubes via a hybrid process of iCVD and template removal. Porous membranes were used as the templates for the deposition of poly(methacrylic acid-*co*-ethylene glycol diacylate). The biomimetic mineralization of nanotubes was conducted to obtain apatite/nanotube composites with structure resembling that of the natural bone.

Chapter V is the conclusion related to previous chapters along with the suggestions for further work.

1.6 References

1. L.S. Nair and C.T. Laurencin, *Progress in Polymer Science*, 2007, **32**, 762-798.
2. N.A. Peppas and R. Langer, *Science*, 1994, **263**, 1715-1720.
3. F.D. Ingraham, E. Alexander and D.D. Matson, *New England Journal of Medicine*, 1947, **236**, 362-368.
4. O. Wichterle and D. Lim, *Nature*, 1960, **185**, 117-118.
5. O. Wichterle, *Soft Contact Lens*, ed. R. M.1978, New York: Wiely. 3-5.
6. O. Wichterle, *US Patent 3316858*, 1968: US.
7. M. Dreifus and L. Klenka, *Ceskoslovenska Oftalmologie*, 1959, **15**, 95-101.
8. M. Dreifus, O. Wichterle and D. Lim, *Ceskoslovenska Oftalmologie*, 1960, **16**, 154-159.
9. M. Dreifus, T. Herben, D. Lim and O. Wichterle, *Sbornik Lekařsky*, 1960, **62**, 212-218.
10. H.M. Lee, J.K. Kim and T.S. Cho, *Bull. Korean Chem. Soc*, 2011, **32**, 4239.
11. R. Langer and N.A. Peppas, *AIChE Journal*, 2003, **49**, 2990-3006.
12. M. Torres-Lugo, M. García, R. Record and N.A. Peppas, *Journal of Controlled Release*, 2002, **80**, 197-205.
13. J. Zhang and N.A. Peppas, *Macromolecules*, 2000, **33**, 102-107.
14. F. Xu, K. Neoh and E. Kang, *Progress in Polymer Science*, 2009, **34**, 719-761.
15. T. Ravikumar, H. Murata, R.R. Koepsel and A.J. Russell, *Biomacromolecules*, 2006, **7**, 2762-2769.
16. J. Huang, H. Murata, R.R. Koepsel, A.J. Russell and K. Matyjaszewski, *Biomacromolecules*, 2007, **8**, 1396-1399.
17. F. Yao, G.D. Fu, J. Zhao, E.T. Kang and K.G. Neoh, *Journal of Membrane Science*, 2008, **319**, 149-157.
18. S.B. Lee, R.R. Koepsel, S.W. Morley, K. Matyjaszewski, Y. Sun and A.J. Russell, *Biomacromolecules*, 2004, **5**, 877-882.

19. H. Murata, R.R. Koepsel, K. Matyjaszewski and A.J. Russell, *Biomaterials*, 2007, **28**, 4870-4879.
20. D. Schmaljohann, *Advanced Drug Delivery Reviews*, 2006, **58**, 1655-1670.
21. Y. Ye and Y. Mao, *J. Mater. Chem.*, 2011, **21**, 7946-9852.
22. J.M. Anderson, *Cardiovascular Pathology*, 1993, **2**, 33-41.
23. B.D. Ratner and S.J. Bryant, *Annu. Rev. Biomed. Eng.*, 2004, **6**, 41-75.
24. E. Merrill, E. Salzman, B. Lipps Jr, E. Gilliland, W. Austen and J. Joison, *ASAIO Journal*, 1966, **12**, 139.
25. R. Britton, E. Merrill, E. Gilliand, E. Salzman, W. Austen and D. Kemp, *Journal of Biomedical Materials Research*, 1968, **2**, 429-441.
26. E. Merrill, E. Salzman, P. Wong, T. Ashford, A. Brown and W. Austen, *Journal of Applied Physiology*, 1970, **29**, 723.
27. G.H. Gifford Jr, E.W. Merrill and M.S. Morgan, *Journal of Biomedical Materials Research*, 1976, **10**, 857-865.
28. E. Merrill and E. Salzman, *ASAIO Journal*, 1983, **6**, 60-64.
29. J.M. Harris, ed. *Poly(ethylene glycol) Chemistry: Biotechnical and Biomedical applications*, 1992, Plenum Press: New York.
30. E. Ostuni, R.G. Chapman, R.E. Holmlin, S. Takayama and G.M. Whitesides, *Langmuir*, 2001, **17**, 5605-5620.
31. G.B. Sigal, M. Mrksich and G.M. Whitesides, *Journal of the American Chemical Society*, 1998, **120**, 3464-3473.
32. G. Li, H. Xue, C. Gao, F. Zhang and S. Jiang, *Macromolecules*, 2010, **43**, 14.
33. R.E. Holmlin, X. Chen, R.G. Chapman, S. Takayama and G.M. Whitesides, *Langmuir*, 2001, **17**, 2841-2850.
34. G. Cheng, Z. Zhang, S. Chen, J.D. Bryers and S. Jiang, *Biomaterials*, 2007, **28**, 4192-4199.
35. J. Ladd, Z. Zhang, S. Chen, J.C. Hower and S. Jiang, *Biomacromolecules*, 2008, **9**, 1357-1361.
36. Z. Zhang, H. Vaisocherová, G. Cheng, W. Yang, H. Xue and S. Jiang, *Biomacromolecules*, 2008, **9**, 2686-2692.
37. S. Weiner and H.D. Wagner, *Annual Review of Materials Science*, 1998, **28**, 271-298.
38. Q. Liu, J. Ding, F.K. Mante, S.L. Wunder and G.R. Baran, *Biomaterials*, 2002, **23**, 3103-3111.
39. J.D. Hartgerink, E. Beniash and S.I. Stupp, *Science*, 2001, **294**, 1684.
40. D.W. Hutmacher, *Biomaterials*, 2000, **21**, 2529-2543.
41. J.D. Hartgerink, E. Beniash and S.I. Stupp, *Science*, 2001, **294**, 1684-1688.
42. Y. Yokoyama, A. Oyane and A. Ito, *Journal of Biomedical Materials Research Part B: Applied Biomaterials*, 2008, **86**, 341-352.
43. H.S. Yu, J.H. Jang, T.I. Kim, H.H. Lee and H.W. Kim, *Journal of Biomedical Materials Research Part A*, 2009, **88**, 747-754.
44. P.A. Madurantakam, I.A. Rodriguez, C.P. Cost, R. Viswanathan, D.G. Simpson, M.J. Beckman, P.C. Moon and G.L. Bowlin, *Biomaterials*, 2009, **30**, 5456-5464.
45. S.S. Kim, M.S. Park, S.J. Gwak, C.Y. Choi and B.S. Kim, *Tissue engineering*, 2006, **12**, 2997-3006.
46. A. Tampieri, S. Sprio, M. Sandri and F. Valentini, *Trends in Biotechnology*, 2011.

47. M.E. Alf, A. Asatekin, M.C. Barr, S.H. Baxamusa, H. Chelawat, G. Ozaydin‐Ince, C.D. Petruczok, R. Sreenivasan, W.E. Tenhaeff and N.J. Trujillo, *Advanced Materials*, 2010, **22**, 1993-2027.
48. H.O. Pierson, 1999: William Andrew.
49. M. Ma, M. Gupta, Z. Li, L. Zhai, K.K. Gleason, R.E. Cohen, M.F. Rubner and G.C. Rutledge, *Advanced Materials*, 2007, **19**, 255-259.

CHAPTER II

INHIBITION OF BACTERIA ADHESION ON VAPOR DEPOSITED POLYAMPHOLYTE COATINGS

Abstract

Antifouling surfaces were achieved using polyampholytes of poly (methacrylic acid-*co*-2-dimethylamino ethyl methacrylate-*co*-ethylene glycol diacrylate) (PMDE) synthesized via initiated chemical vapor deposition (iCVD) without further treatment. The ratio of cationic methacrylic acid (MAA) units to anionic 2-dimethylamino ethyl methacrylate (DMAEMA) units was varied in the polyampholyte composition. The coatings were subjected to bacteria adhesion and accumulation tests at pH 5-7. Results showed that the polymer surfaces highly resisted bacteria adhesion and inhibited biofilm growth. This may be attributed to two mechanisms: charge dominated resistance at higher pH around 7 and zwitterionic-property dominated resistance at lower pH around 5. The iCVD synthesis of ampholytic polymer coatings provides a promising nonfouling approach for biomedical applications.

2.1 Introduction

Failure of implants such as protheses and sensors due to bacteria accumulation has attracted much attention in recent years. Therefore, permanent bacteria-killing surfaces have been developed using various methods, such as atom radical transfer polymerization [1-3], surface derivation [4], UV-introduced graft copolymerization [5] and initiated chemical vapor deposition [6]. Although bacteria-killing purpose was achieved, the adsorbed dead bacteria could still lead to invalidation of antibacterial coatings. To resolve this problem, a switchable biocompatible polymer surface was reported, which had both self-sterilizing and nonfouling capabilities [7]. However, the surface needed to be immersed in a strong basic solution (pH 10) to release the adsorbed dead bacteria.

Another approach is to create an antifouling thin film that resists bacteria adhesion. Several materials were reported effective to resist bacteria and applicable to biosensors [8], medical implants [9] and drug-delivery carriers [10]. Among these materials, poly(ethylene glycol) (PEG) is the most wildly used antifouling material [11]. However, for long term applications, oxidation damage and enzymatic cleavage of PEG chains result in degradation of chains and loss of antifouling properties [12-14]. Zwitterionic polymers have been considered as another candidate for antifouling applications [15]. Polyphosphobetaine and polysulfobetaine coatings were synthesized and the capabilities of bacteria resistance were demonstrated [16]. Atom transfer radical polymerization (ATRP) was used to synthesize thin films of poly (sulfobetaine methacrylate) (PSBMA) and poly (carboxylbetaine methacrylate) (PCBMA), which inhibited bacteria adhesion, biofilm formation and protein adsorption [17, 18, 40-43]. ICVD of poly(2-dimethylamino ethyl methacrylate-*co*-ethylene glycol dimethacrylate) combined with 1,3-propane

sultone surface treatment was used to fabricate a zwitterionic film, which was resistant to bacteria adhesion as well [19].

The high resistance to bacteria/protein adsorption is attributed to the surface hydration introduced by electric forces between water molecules and surface functional groups on antifouling coatings [20-22]. Polyampholytes, containing cationic and anionic groups, which also can effectively introduce surface hydration, have potential antifouling capability. However, not much research has focused on antifouling properties of polyampholytes. A series of polyampholytes with homogenously mixed charge were synthesized and their high protein resistance was reported [23]. Another nonfouling polyampholyte was synthesized via ATRP from an ion-pair comonomer with biomimetic adhesive groups, but the amount of cationic and anionic moieties had to be exactly 1:1 [24]. Heterogeneous charged ampholytic polymer has barely been investigated for its antifouling functionality.

Current approaches in preparing antifouling materials include ATRP [17, 18, 24], self-assembled monolayers (SAMs) [25, 26] and solution polymerization, solvent evaporation [27], and initiated chemical vapor deposition (iCVD) [19]. Among these methods, iCVD has many advantages over the others, such as high conformality, easy control of thickness, no requirement of surface functionality and no use of solvents [19]. In addition, iCVD technique is performed at low operating pressures and temperatures under an all-dry environment, making it promising for surface modification [28]. So far, the synthesis of nonfouling polyampholytic coatings has not been reported using a vapor-based method.

In this study, polymers containing opposite charges from 2-dimethylamino ethyl methacrylate (DMAEMA) and methacrylic acid (MAA) were synthesized using iCVD. The nonfouling properties of ampholytic polymers were studied for the first time. The ratios of cationic groups to anionic groups were varied and ethylene glycol diacrylate (EGDA) was used as cross-linker to improve polymer stability. The polymer compositions were characterized using Fourier Transform Infrared (FTIR). The examinations of antifouling capabilities of polyampholytes for short-term and long-term applications were conducted. *Escherichia coli* (*E. coli*) were used to test both bacteria adhesion and accumulation.

2.2 Experimental

2.2.1 Materials

EGDA (90%), DMAEMA (98%), MAA (99%), and tert-butyl peroxide (TBP) (98%) were all purchased from Sigma-Aldrich Chemical Co. (St. Louis, MO) and directly employed without further purification. Silicon wafers were purchased from MEMC Electronic Materials (St. Peters, MO). Plastic microscopy slides with the size of 60mm×24mm were purchased from Electron Microscopy Science (Hatfield, PA). Glass slides and plastic slides were cleaned using 70% ethanol before vapor deposition and, together with silicon wafers, were used as planar substrates during hydrogel coating deposition.

2.2.2 Synthesis

All iCVD depositions of polyampholyte films were carried out in a custom built reactor (Sharon Vacuum) as previously described [6, 29]. The reactor, which covered with a quartz plate, was 25 cm in diameter. It was equipped with parallel Nichrome filament array (Ni80/Cr20, Goodfellow) 2.5 cm above the deposition stage, which was maintained a certain temperature using water cooling. The temperatures of the filaments and stage were measured using thermocouples (Omega, Type K) attached to them. During iCVD deposition, the initiator was fed at room temperature, while the EGDA, MAA and DMAEMA monomers were heated to 60 ℃, 45 ℃ and 55 ℃ in glass jars, respectively. The vapor was delivered through mass flow controllers (MKS Instruments, model 1479A, 1150 and 1153) and mixed in the reactor. The flow rate of initiator TBP was set constant at 0.4 sccm, while the flow rates of EGDA, MAA and DMAEMA were varied to obtain polymer coatings with different compositions. In order to enhance the stability of polymer coatings and effective components on the surface, hybrid grafting was deployed and proceeded as the following three stages. The feeding rates and controlled thickness of poly(methacrylic acid-*co*-2-dimethylamino ethyl methacrylate-*co*-ethylene glycol diacrylate) (PMDE), poly(methacrylic acid-*co*- ethylene glycol diacrylate) (PME) and poly(2-dimethylamino ethyl methacrylate-*co*-ethylene glycol diacrylate) (PDE) coatings in each stage are listed in Table 2.1. PMDE-1 and PMDE-2 were two polyampholyte coatings, which contained MAA, DMAEMA and EGDA. PME was negatively charged coating containing MAA and EGDA, while PDE was positively charged coating consisting of DMAEMA and EGDA. The filaments were resistively heated to 220 ℃ and the temperature of the stage was kept at 38-45 ℃ during deposition. The pressure inside the vacuum chamber was maintained at 0.25 Torr during the

deposition by a throttling butterfly valve (MKS, Type 253B). The growth of the polymer coatings on the reference surface of a Si wafer was monitored real time using in-situ interferometry with a 633 nm He-Ne laser (JDS Uniphase). Glass slides and plastic slides were both used as substrate materials.

Table 2.1 Deposition conditions of PMDE, PME, and PDE coatings.

		Flow rate/sccm			Thickness/nm
		MAA	DMAEMA	EGDA	
PMDE-1	Stage I	0	0	0.83	100
	Stage II	0.83	1.66	0.83	900
	Stage III	0.83	1.66	0	100
PMDE-2	Stage I	0	0	0.83	100
	Stage II	1.66	0.83	0.83	900
	Stage III	1.66	0.83	0	100
PME	Stage I	0	0	0.66	100
	Stage II	2.03	0	0.66	900
	Stage III	2.03	0	0	100
PDE	Stage I	0	0	0.66	100
	Stage II	0	2.03	0.66	900
	Stage III	0	2.03	0	100

After deposition, the polyampholyte coatings were characterized using Fourier Transform Infrared (FTIR). The spectra of the polyampholyte coatings were collected by a Nicolet 6700 spectrometer using a DTGS detector under the transmission mode at 4 cm^{-1} resolution.

2.2.3 Swelling test

To investigate the swelling degree, the water uptake of each polyampholyte coatings at different pH was measured. The thickness of the polymer coatings was approximately 1.1 μm. Before the tests, each polymer coating was soaked in deionized water for 5 min to remove grafted and uncrosslinked component. The weight of the dry-state polymer coating was measured by subtracting the substrate weight before deposition from the coated substrate weight. In each swelling test, a polyampholyte coating was immersed in NaH_2PO_4/Na_2HPO_4 buffer solution at a certain pH (pH 3, 4, 5, 6, 7, and 8) over a certain period of time (3 min, 6 min and 1 hr). After removing the coating out of solution, a wetted filter paper was used to remove the excess water on the coating surface. Then the weight of the hydrated coating was measured. For each coating composition, at least four measurements were taken in different pH buffer solutions. Swelling degree was calculated as SD= $(W-W_0)/W_0$, where W is the hydrated coating weight and W_0 is the dry-state coating weight.

2.2.4 Bacteria adhesion tests

Recombinant *E. coli* bacteria expressing green fluorescent protein (GFP) was used to investigate the nonfouling properties. A single colony of recombinant *E. coli* was inoculated into Luria-Bertani (LB) medium mixed with ampicillin and cultured overnight

at 37 ℃. The bacteria solution was diluted to a bacteria concentration of 10^7 cells/ml with PBS solutions of different pH values (pH 5, 6, 7). Prior to the test, polyampholyte coatings were soaked in deionized water to remove any uncrosslinked component. Afterward, each sample (24mm×20mm) was immersed in 15 ml of 10^7 cells/ml bacteria suspensions and incubated at 37 ℃ for 1 hr. The samples were then taken out and washed with phosphate buffered saline (PBS) solution three times and observed under an Olympus BX51 epifluorescence microscope using a green filter (excitation/emission 440–480 nm/515–540 nm). For the quantitative analysis, ten images were taken for each sample and analyzed using Image J software.

2.2.5 Bacteria viability tests

Samples were removed and washed with PBS solution three times after 1-hr incubation in bacteria suspension. Afterward, they were placed in ampicillin containing LB medium and cultured under 37 ℃ for 24 hr. Samples were washed three times and observed under an Olympus BX51 epifluorescence microscope.

2.3 Results and discussion

2.3.1 Characterization of polyampholytes

The spectra of four polyampholyte coatings are illustrated in Figure 2.1. The spectra of polyampholytes (PMDE-1 and PMDE-2) show the characteristic peaks of MAA and DMAEMA. The broad peaks at 3430 cm^{-1} corresponded to carboxyl (-COOH) groups of MAA, while the C=O stretching absorption from all of three monomers (EGDA, MAA, and DMAEMA) centered in the range from 1735 to 1725 cm^{-1}.

Compared with the spectra of PME and PDE, the spectra of two polyampholytes had new peaks at 1570 cm^{-1}, which indicated the intermolecular interaction between the amino group and the carboxyl group [30].

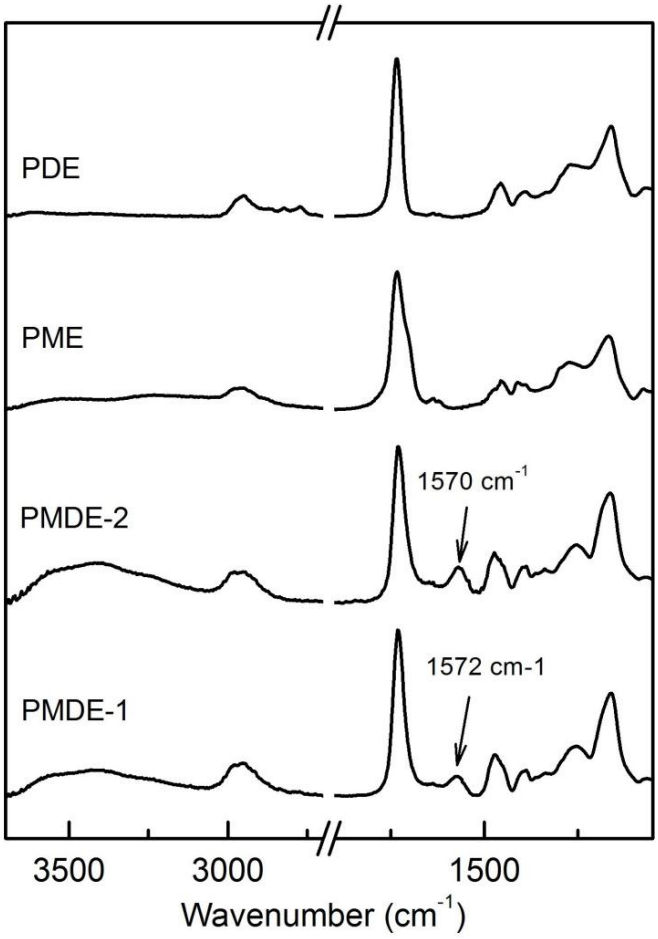

Figure 2.1 FTIR spectra of vapor-deposited PMDE-1, PMDE-2, PME and PDE films.

The quantification of polymer composition was calculated using FTIR analysis. FTIR spectra of PMDE-1, PMDE-2, PME, PDE, PEGDA, PMAA and PDMAEMA were normalized to the thickness of each coating. The decoupling of peaks was carried out using the Peak Resolve tool in Omnic software, and the peak areas of the C=O stretching

in MAA at 1702 cm^{-1}, in DMAEMA at 1728 cm^{-1} and in EGDA at 1735 cm^{-1} were measured. According to the Beer-Lambert Law, the absorbance peak area of the C=O stretching was proportional to unit concentration and the corresponding absorption coefficient. Verified by previous studies on other acrylic copolymers [31], the assumption was made that the adsorption coefficients of the C=O stretching were the same in the PMDE, PME, and PDE as in PMAA and PDMAEMA homopolymers, respectively. The mole concentration of each component in each copolymer (C) to the component in its corresponding homopolymer (C^*) can be calculated using: $C/C^*=A_{C=O}/A^*_{C=O}$, where $A_{C=O}$ and $A^*_{C=O}$ are the peak area of the C=O absorption in the spectra of copolymer and homopolymer, respectively. Thus, mole concentration of each component (C) can be calculated as: $C= C^* \cdot A_{C=O}/A^*_{C=O}$. Since mole concentration can be derived from the molecular mass of monomer (M) and density (ρ), C equals $\rho \cdot A_{C=O}/M \cdot A^*_{C=O}$. The molar ratio of MAA units to DMAEMA units in each polymer coating $n_{MAA} : n_{DMAEMA}$ is equal to $C_{MAA} : C_{DMAEMA}$ and can be calculated under the assumption of equal density in each coating:

$$n_{MAA} : n_{DMAEMA} = \frac{A_{C=O(MAA)}}{M_{MAA}A^*_{C=O(MAA)}} : \frac{A_{C=O(DMAEMA)}}{M_{DMAEMA}A^*_{C=O(DMAEMA)}}$$

The n_{MAA}/n_{DMAEMA} of PMDE-1 and PMDE-2was was calculated to be 0.22 and 0.31, respectively. It was noted that the amount of MAA in polyampholytes is less than DMAEMA even at high feeding ratio of MAA to DMAEMA.

2.3.2 Degree of swelling

It is believed that zwitterionic polymers have good nonfouling capabilities due to their charge neutrality and surface hydration via hydrogen bonding introduced by electrostatic effect [15]. At the isoelectric point (pI) of ampholytic polymer, it exhibits the same electrostatic property as zwitterionic polymer and the electrostatic forces lead to minimal swelling by electric attraction between positive and negative moieties.

Based on the physical behavior of polyampholytic coatings at different pH, a series of pH-dependent swelling tests were done on the polyampholytes (PMDE-1 and PMDE-2) and polyelectrolytes (PME and PDE). Figure 2.2 shows the swelling degree of each polymer in buffer solution for 1 hr. The swelling degree of PDE film decreased with the increase of pH, while that of PME film increased slightly as pH increased. The minimal swelling degree of both polyampholytes was at around pH 5, which indicated the range of pI of the synthesized polyampolytes. At pH higher than pH 5, the swelling degree of polyampholytes increased as pH increased, while at pH lower than pH 5, DS of polyampholytes decreased as pH increased. The minor difference of composition did not influence the trend of swelling, and the pI of polyampholytes, which contained fewer anionic units, was below pH 7. More steady ionization of MAA than DMAEMA may be the reason [32]. The higher swelling degree of PMDE-1 than PMDE-2 was attributed to composition difference: there were more DMAEMA units relative to MAA units in PMDE-1 than PMDE-2 [33, 34].

The polyelectrolytes are considered to have high swelling degree because of the strong repulsion between same charged groups in molecules. It was evident in Figure 2.2, however, that the swelling degree of polyelectrolytes was much lower than polyampholytes at pH 3 to 8, even around the pI of polyampholytes.

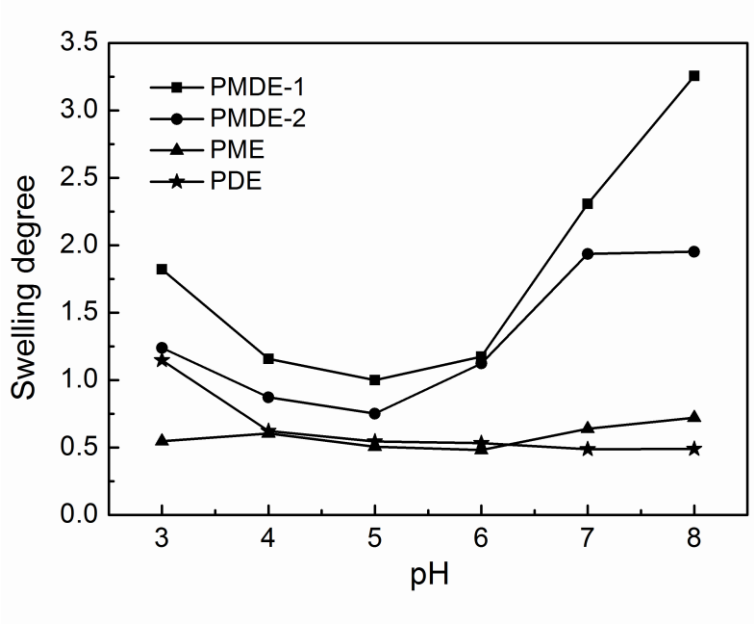

Figure 2.2 The swelling degree of PMDE-1, PMDE-2, PME and PDE coatings at different pH.

The swelling degree, in terms of surface hydration, is considered as one factor in bacteria adhesion tests. Therefore, two different substrates coated with the same coatings of PMDE-2 were used to study the influence of nonfouling behavior with different swelling degree. As seen in Figure 2.3, the swelling degree of PMDE-2 on the plastic plate immersed for 1 hr was lower than that on the glass slide immersed for 3 min, except at pH 5. This is because the glass surface is more hydrophilic than the plastic surface, which allows water molecules to penetrate the polymer coating more easily. Hence, it is logically concluded that during the 1-hr bacteria adhesion tests, the swelling degree of polymer coating on the glass should be higher than that on the plastic. The tests of short-term bacteria adhesion were taken on both PMDE-2 deposited substrates in 10^7 cells/ml *E. coli* solutions at pH 7. There is no obvious difference in bacteria resistance exhibited by

images in Figure 2.3, which suggests that the surface hydration degree is not the major factor influencing the nonfouling properties of polyampholyte coatings in this study. In other words, the hydration degree of polyampholytes coated on plastic plates is high enough to inhibit bacteria adhesion. In the following bacteria adhesion studies, plastic plates were chosen as substrates due to the fact that polymer coatings were more stable on the plastic plates.

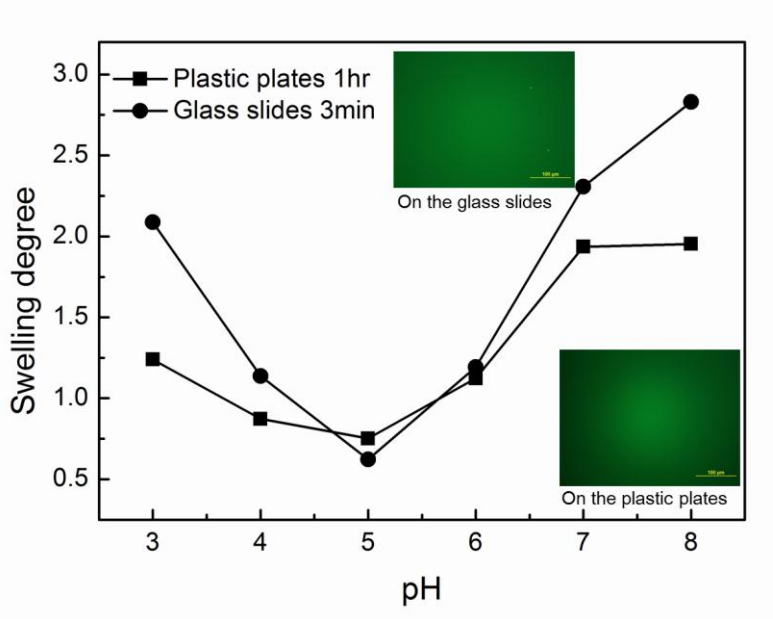

Figure 2.3 The swelling degree of PMDE-2 coatings vapor-deposited on two different substrates (plastic plates and glass slides) after immersed 1 hr and 3 min in buffer solutions at different pH, respectively. The images of bacteria adhesion show bacteria adhesion at pH7.

2.3.3 Short-term bacteria adhesion studies

Short-term bacteria adhesion tests at pH 7 were undertaken on the surfaces of PMDE-1, PMDE-2, PME, PDE coatings and control plastic plates for 1 hr. The reduction of bacteria adhesion was calculated as: Reduction=$(N_{control}-N_{polymer})/N_{control}\times 100\%$, where

$N_{control}$ and $N_{polymer}$ were the number of adhered bacteria on the control plates and on the polymer coating. Bacteria reductions, exhibited quantitatively as the reduction of bacteria adhesion relative to control, are shown in Figure 2.4. More than 99% of bacteria on the polyampholytes and about 94% of bacteria on the PME surface were reduced at pH 7, while there were more bacteria adhering to the surfaces of PDE than control plates.

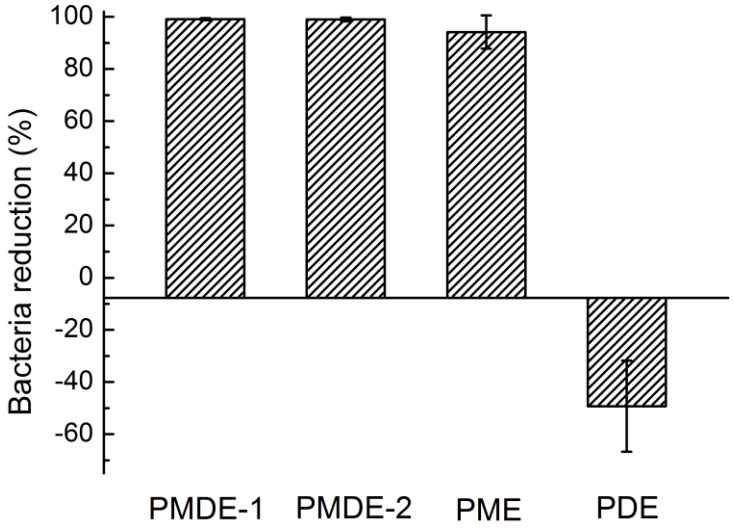

Figure 2.4 The reduction of bacteria adhesion on the polymeric surfaces after 1-hr incubation in *E. coli* solutions at pH 7.

To study the pH dependence effect of polyampholytes on bacteria resistance, all polymer films were subjected to the short term bacteria adhesion test at pH 5, 6, and 7. As shown in Figure 2.5, the bacteria reductions of PME and PDE increase with the increase of pH values. More than 99% bacteria were reduced on the polyampholytes regardless of the change of pH values and the lines of two polyampholytes in Figure 2.5 were overlapped. For PME and PDE coatings, the trend of bacteria reduction was surface

charge dependent. MAA can ionize to be negatively charged when pH is higher than the pK_a at 5.35 and protonate to be less negative at lower pH; while DMAEMA can protonate to hold positive charge when pH is lower than its pK_b at 8.00 and deprotonate at higher pH [35, 36]. Most bacteria, either Gram-positive or Gram-negative bacteria, have negatively charged surfaces [37]. In this study, *E. coli* with negatively charged surface was used for all tests. Therefore, at higher pH, such as pH 7, repulsive force between negative surfaces of PME coating and *E. coli* led to the higher reduction, while at lower pH, such as pH 5, the attractive force between positive surfaces of PDE and *E. coli* led to the negative reduction. As to polyampholytes, their performance on resistance to bacteria adhesion was not pH-dependent. This can be attributed not only to the surface charge effects, but also to the "zwitterionic property" (electric neutrality) at pI. At pH higher than the pI, polyampholytes are negatively charged since MAA units in the polymer highly ionize to be negative and DMAEMA units deprotonate to be less positive; this can be named "charge dominated resistance" (CDR). At pH around the pI, polyampholytes perform as zwitterionic polymers; this can be named "zwitterionic-property dominated resistance" (ZDR). Thus, the combination of CDR and ZDR effects resulted in high resistance to bacteria adhesion and wider pH range for polyampholytes, which enhances their nonfouling performance. This resolves the problem that zwitterionic polymers have [38]. Zwitterionic polymers maintain electric neutrality at around pH 7. When pH is decreased, they become partially protonated, which in turn compensates the electrostatic neutrality at low pH and therefore resulting in bacteria absorption.

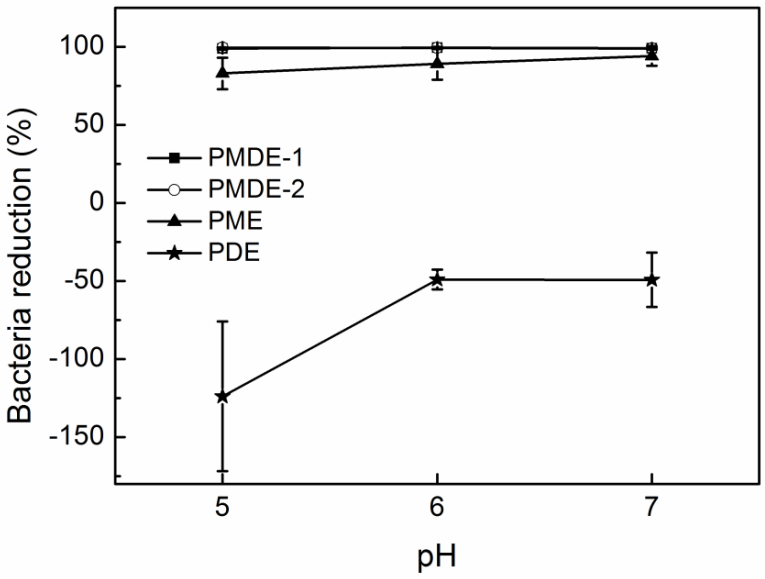

Figure 2.5 The reduction of *E. coli* bacteria adhesion at pH 5, 6 and 7 on the surfaces of PMDE-1, PMDE-2, PME and PDE coatings.

2.3.4 Long-term bacteria viability

Long-term bacteria accumulation tests in ampicillin containing LB media were performed on the surfaces of PMDE-1, PMDE-2, PME, and PDE. Figure 2.6B shows the representative qualitative images of accumulated *E. coli* on the above materials' surfaces. No biofilm accumulation was observed on the surfaces of both PMDE-1 and PMDE-2 over 24-hr period, while biofilm of *E. coli* formed on the surfaces of PME, PDE, and control plates. Compared with the qualitative images of 1-hr bacteria adhesion on PMDE-1, PMDE-2, PME, PDE and control plates surfaces (Figure 2.6), after 24-hr incubation rapid growth of bacteria on PME, PDE and control plate surfaces was observed, while the surfaces of PMDE-1 and PMDE-2 were still clean. The excellent performance of PMDE-1 and PMDE-2 on drastic reduction of the accumulation of *E. coli* is due to their ability to

resist bacteria adhesion. The bacteria adhesion experiments showed that fewer *E. coli* were adhering to PMDE-1 and PMDE-2 surfaces than two polyelectrolytes. The nonfouling capability is still effective to discourage the biofilm formation on polyampholytes. The bacteria accumulation of *E. coli* on PME and control plate was proportional to the amount of adhesion of *E. coli* in short-term test. From the fluorescence microscopy, it was visibly observed that there was less growth of biofilm on the PDE than on the control. The phenomenon that PDE exhibited the highest bacteria attachment in 1-hr study while less biofilm growth in the 24-hr study was consistent with the conclusion in Gottenbos's study that positively charged surface may impede the growth of bacteria due to its strong electrostatic attraction of organisms though it is adhesive to bacteria [39].

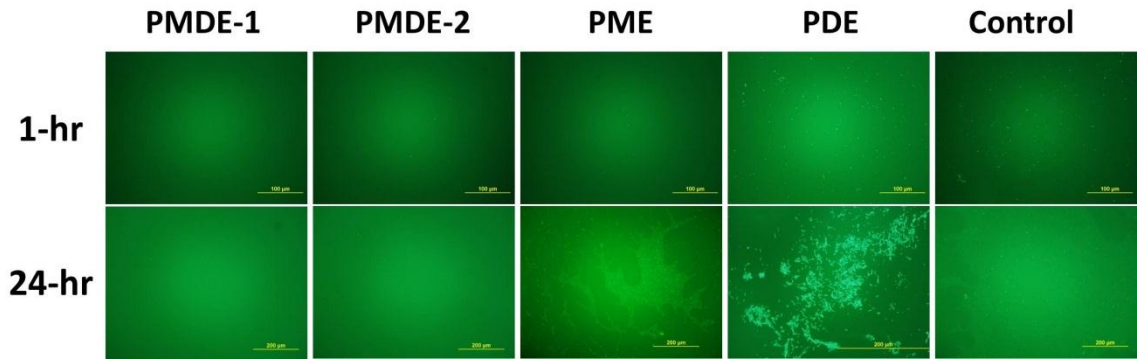

Figure 2.6 Bacteria adhesion at pH 7 after 1-hr and 24-hr incubation.

2.4 Conclusion

PMDE polyampholyte synthesized via iCVD can be an alternate nonfouling coating for biomedical applications. From the swelling tests, these polyampholytes exhibited electroneutral properties as zwitterionic polymer at pI of pH 5. Polyampholytes were subjected to the bacteria adhesion and accumulation tests. The results showed that more than 99% of bacteria adhesion was reduced on the polyampholytic surfaces at pH 7. The bacteria resistance of polyampholytes was pH independent. Synthesized polyampholytes coating effectively discouraged biofilm formation after 24-hr incubation.

2.5 References

1. S.B. Lee, R.R. Koepsel, S.W. Morley, K. Matyjaszewski, Y.J. Sun and A.J. Russell, *Biomacromolecules*, 2004, **5**, 877-882.
2. H. Murata, R.R. Koepsel, K. Matyjaszewski and A.J. Russell, *Biomaterials*, 2007, **28**, 4870-4879.
3. S. Lenoir, C. Pagnoulle, C. Detrembleur, M. Galleni and R. Jerome, *Journal of Polymer Science Part a-Polymer Chemistry*, 2006, **44**, 1214-1224.
4. J.C. Tiller, C.J. Liao, K. Lewis and A.M. Klibanov, *Proceedings of the National Academy of Sciences of the United States of America*, 2001, **98**, 5981-5985.
5. L. Cen, K.G. Neoh and E.T. Kang, *Langmuir*, 2003, **19**, 10295-10303.
6. Y.M. Ye, Q. Song and Y. Mao, *Journal of Materials Chemistry*, 2011, **21**, 257-262.
7. G. Cheng, H. Xite, Z. Zhang, S.F. Chen and S.Y. Jiang, *Angewandte Chemie-International Edition*, 2008, **47**, 8831-8834.
8. K.L. Prime and G.M. Whitesides, *Science*, 1991, **252**, 1164-1167.
9. B.D. Ratner and S.J. Bryant, *Annual Review of Biomedical Engineering*, 2004, **6**, 41-75.
10. R. Langer, *Science*, 2001, 58-59.
11. J.M. Harris, ed. *Poly(ethylene glycol) Chemistry: Biotechnical and Biomedical applications*, 1992, Plenum Press: New York.
12. S. Krishnan, C.J. Weinman and C.K. Ober, *Journal of Materials Chemistry*, 2008, **18**, 3405-3413.
13. E. Ostuni, R.G. Chapman, R.E. Holmlin, S. Takayama and G.M. Whitesides, *Langmuir*, 2001, **17**, 5605-5620.

14. V. Gaberc-Porekar, I. Zore, B. Podobnik and V. Menart, *Current Opinion in Drug Discovery & Development*, 2008, **11**, 242-250.
15. S.Y. Jiang and Z.Q. Cao, *Advanced Materials*, 2010, **22**, 920-932.
16. S.L. West, J.P. Salvage, E.J. Lobb, S.P. Armes, N.C. Billingham, A.L. Lewis, G.W. Hanlon and A.W. Lloyd, *Biomaterials*, 2004, **25**, 1195-1204.
17. G. Cheng, Z. Zhang, S.F. Chen, J.D. Bryers and S.Y. Jiang, *Biomaterials*, 2007, **28**, 4192-4199.
18. J. Ladd, Z. Zhang, S. Chen, J.C. Hower and S. Jiang, *Biomacromolecules*, 2008, **9**, 1357-1361.
19. R. Yang, J.J. Xu, G. Ozaydin-Ince, S.Y. Wong and K.K. Gleasont, *Chemistry of Materials*, 2011, **23**, 1263-1272.
20. S.F. Chen, J. Zheng, L.Y. Li and S.Y. Jiang, *Journal of the American Chemical Society*, 2005, **127**, 14473-14478.
21. Y. He, J. Hower, S.F. Chen, M.T. Bernards, Y. Chang and S.Y. Jiang, *Langmuir*, 2008, **24**, 10358-10364.
22. S.F. Chen, L.Y. Li, C. Zhao and J. Zheng, *Polymer*, 2010, **51**, 5283-5293.
23. S. Chen and S. Jiang, *Advanced Materials*, 2008, **20**, 335-338.
24. G.Z. Li, H. Xue, C.L. Gao, F.B. Zhang and S.Y. Jiang, *Macromolecules*, 2010, **43**, 14-16.
25. S. Chen, F. Yu, Q. Yu, Y. He and S. Jiang, *Langmuir*, 2006, **22**, 8186-8191.
26. R.E. Holmlin, X.X. Chen, R.G. Chapman, S. Takayama and G.M. Whitesides, *Langmuir*, 2001, **17**, 2841-2850.
27. H. Kitano, T. Mori, Y. Takeuchi, S. Tada, M. GemmeiIde, Y. Yokoyama and M. Tanaka, *Macromolecular Bioscience*, 2005, **5**, 314-321.
28. S.H. Baxamusa, S.G. Im and K.K. Gleason, *Phys. Chem. Chem. Phys.*, 2009, **11**, 5227-5240.
29. Y.M. Ye and Y. Mao, *Journal of Materials Chemistry*, 2011, **21**, 7946-7952.
30. L.D. Deng, Y.L. Zhai, S.T. Guo, F.M. Jin, Z.P. Xie, X.H. He and A.J. Dong, *Journal of Nanoparticle Research*, 2009, **11**, 365-374.
31. K. Chan and K.K. Gleason, *Langmuir*, 2005, **21**, 8930-8939.
32. S. Wen and W. Stevenson, *Colloid & Polymer Science*, 1993, **271**, 38-49.
33. S.H. Yuk and S.H. Cho, *European Polymer Journal*, 2001, **37**, 1985-1989.
34. R. Toomey, D. Freidank and J. Ruhe, *Macromolecules*, 2004, **37**, 882-887.
35. Y. Merle, *Journal of Physical Chemistry*, 1987, **91**, 3092-3098.
36. A.B. Lowe and C.L. McCormick, *Chemical Reviews*, 2002, **102**, 4177-4189.
37. B.A. Jucker, H. Harms and A.J.B. Zehnder, *Journal of Bacteriology*, 1996, **178**, 5472-5479.
38. Z. Zhang, H. Vaisocherová, G. Cheng, W. Yang, H. Xue and S. Jiang, *Biomacromolecules*, 2008, **9**, 2686-2692.
39. B. Gottenbos, D.W. Grijpma, H.C. Van Der Mei, J. Feijen and H.J. Busscher, *Journal of Antimicrobial Chemotherapy*, 2001, **48**, 7.
40. G. Cheng, G. Li, H. Xue, S. Chen, J.D. Bryers and S. Jiang, *Biomaterials*, 2009, **30**, 5234-5240.
41. G. Li, G. Cheng, H. Xue, S. Chen, F. Zhang and S. Jiang, *Biomaterials*, 2008, **29**, 4592-4597.

42. I. Banerjee, R.C. Pangule and R.S. Kane, *Advanced Materials*, 2011, **23**, 690-718.
43. A.J. Keefe and S. Jiang, *Nature Chemistry*, 2011, **4**, 59-63.

CHAPTER III

ANTIFOULING EFFECTS OF POSITIVELY CHARGED SURFACES

Abstract

Bacteria adhesion and accumulation on biomedical device surfaces cause infection problems. Among polymeric biomaterial surfaces, positively charged surfaces are believed to be effective in promoting bacteria adhesion. Herein, a study on the antifouling effects of positively charged surfaces was carried out. Copolymers poly(2-dimethylamino ethyl methacrylate-*co*-ethylene glycol diacrylate) (PDE) synthesized via iCVD were used as positively charged surfaces with different amounts of cationic moieties. Adhesion and growth of *Escherichia coli* on the surfaces were investigated. The results showed that the highest amount of bacteria adhered to PDE-3 surfaces, which had highest density of positive charges, while further bacteria growth was suppressed.

3.1 Introduction

Infection of implanted biomedical devices caused by adhesion and accumulation of bacteria is still a problem for clinical medicine [1]. 5%-15% patients are affected by hospital infections and it causes $ 35.7 billion to $ 45 billion medical costs each year in the United States [9]. In spite of the advantages in design of biomedical devices, including prostheses, orthopedic implants, artificial hearts and so forth, there are no solutions for the infection problem other than removal of the devices. The initiation of infection is bacteria adhesion on the surfaces of biomaterials, followed by bacteria growth and biofilm formation, which cause the failure of biomedical devices. As is known, most bacteria are carrying net negatively charged surfaces [2], hence, the adhesion of bacteria is promoted on the positively charged surfaces due to electric attraction. This is consistent with the observation in the previous chapter as well. However, the infection is mainly caused by the biofilm formation following initial adhesion [3]. Bart Gottenbos *et al* reported that adhesion of Gram-negative bacteria was rapid on a positively charged surface, but further growth was inhibited [4]. The same observation was published by Harkes *et al* for *Escherichia coli* [5].

In this chapter, an investigation on interaction of Gram-negative bacteria and positively charged surfaces of poly (2-dimethylamino ethyl methacrylate-*co*-ethylene glycol diacrylate) (PDE) was conducted. *E. coli* was used as the model bacteria. The ratio of ethylene glycol diacrylate (EGDA) to 2-dimethylamino ethyl methacrylate (DMAEMA) was varied to fabricate surfaces with different densities of positive moieties.

3.2 Experimental

3.2.1 Materials

EGDA (90%), DMAEMA (98%) and tert-butyl peroxide (TBP) (98%) were purchased from Sigma-Aldrich Chemical Co. and used as received. Plastic microscopy slides of 60mm×24mm in size were purchased from Electron Microscopy Science, and cleaned with 70% ethanol before vapor deposition and adhesion tests. Silicon wafers were purchased from MEMC Electronic Materials, together with plastic plates, were used as the planar substrates.

3.2.2 Synthesis

As previously described, a custom built reactor (Sharon Vacuum) was used to perform all iCVD deposition of hydrogel [6]. During iCVD deposition, the initiator TBP was used at room temperature, while the EGDA and DMAEMA monomers were vaporized at 60 ℃ and 55 ℃ in glass jars, respectively. The vapors were pumped into the reactor through mass flow controllers (MKS Instruments, model 1479A and 1153) and were mixed in the vacuum chamber. The flow rate of TBP was 0.4 sccm. To synthesize polymer coatings with different compositions, the flow rates of EGDA and DMAEMA monomers were varied. Hybrid grafting was used to enhance effective components on the surface. The flow rates and coating thickness are listed in Table 3.1. Interferometry with a 633 nm He-Ne laser (JDS Uniphase) was used to monitor the polymer deposition process.

After deposition, the characterization of the polymer coatings was conducted using Fourier Transform Infrared (FTIR). The spectra of the polymer coatings were collected by a Nicolet 6700 spectrometer.

Table 3.1 Deposition conditions of PDE coatings.

		Flow rate/sccm		Thickness/nm
		EGDA	DMAEMA	
PDE-1	Stage I	0.06	0	100
	Stage II	0.06	0.18	900
	Stage III	0	0.18	100
PDE-2	Stage I	0.06	0	100
	Stage II	0.06	0.30	900
	Stage III	0	0.30	100
PDE-3	Stage I	0.06	0	100
	Stage II	0.06	0.60	900
	Stage III	0	0.60	100

3.2.3 Bacteria adhesion tests

A single colony of recombinant *E. coli* that expressed green fluorescent protein (GFP) was inoculated into Luria-Bertani (LB) medium and cultured overnight at 37 ℃. The bacteria solution was diluted to a concentration of 10^7 cells/ml with phosphate

buffered saline (PBS) solutions of different pH values (pH 5, 6, 7). Before test, polymer coatings were soaked in deionized water for 5 min to remove the uncrosslinked component. Each polymer sample (24mm×20mm) was immersed in 15ml of 10^7 cells/ml bacteria suspension of different pH and incubated at 37 ℃ for 1 hr. The samples were removed and washed with bacteria free PBS solution three times. An Olympus BX51 epifluorescence microscope with a green filter (excitation/emission 440–480 nm/515–540 nm) was used to observe bacteria adhesion. To perform the quantitative analysis, 10 images were taken for each sample.

3.2.4 Bacteria growth tests

After being incubated in bacteria suspension for 1 hr and washed three times with PBS solution, polymer coatings were placed into ampicillin containing LB medium with different pH (pH 5, 6 and 7) and cultured at 37 ℃ for 24 hr. Samples were washed three time times with PBS solution and observed under an Olympus BX51 epifluorescence microscope using a green filter.

3.3 Results and discussion

3.3.1 Synthesis of PDE coatings

PDE polymer coatings with different densities of positive charges were synthesized through initiated chemical vapor deposition (iCVD). FTIR spectra of synthesized polymers are shown in Figure 3.1. Desired functional groups were well preserved during deposition. The characteristic peaks of DMAEMA at 2823 and 2774 cm^{-1} were assigned to the C-H stretching in the $–N(CH_3)_2$ groups. In the range from 1735 cm^{-1} to 1725 cm^{-1},

the strong absorption peaks were attributed to the C=O stretching absorption from both DMAEMA and EGDA moieties. In the spectra of PDMAEMA and PEGDA coatings, the peaks of C=O stretching in DMAEMA and EGDA located at 1729 cm^{-1} and 1735 cm^{-1}, respectively [6]. The enlargements of absorption from carbonyl groups in the PDE hydrogels are shown in Figure 3.2. From PDE-1 to PDE-3, the C=O stretching absorption peak gradually shifts from 1733 cm^{-1} to 1731 cm^{-1}, which suggests an increase of the DMAEMA content in the PDE. In addition, the increase of absorption at 2823 cm^{-1} and 2774 cm^{-1} indicates an increase of the DMAEMA moieties in PDE as well.

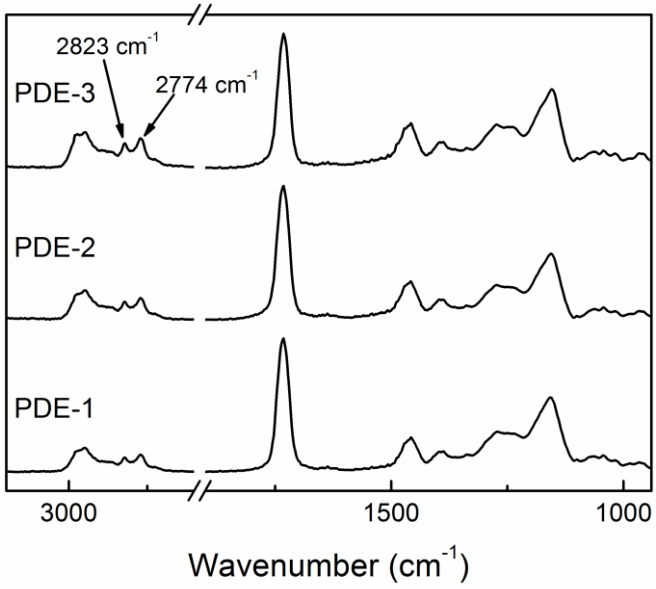

Figure 3.1 FTIR spectra of vapor-deposited PDE-1, PDE-2, and PDE-3 coatings.

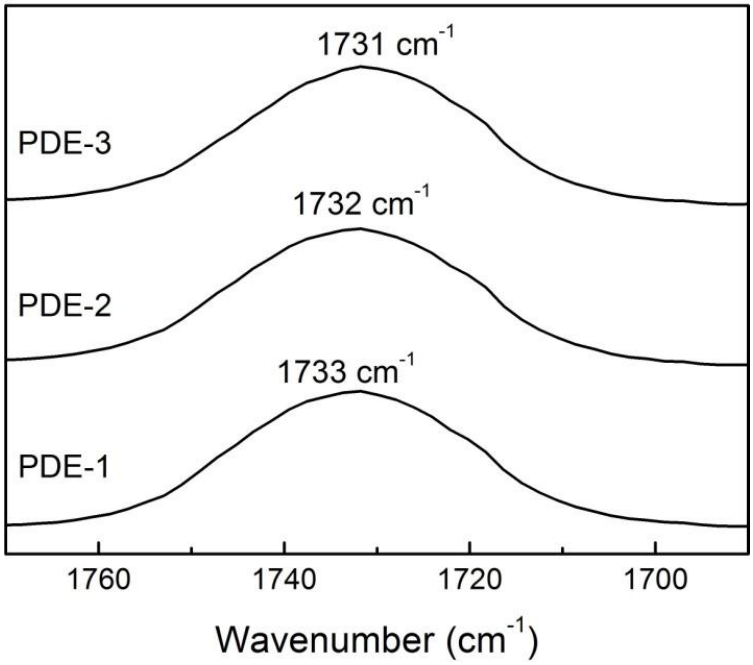

Figure 3.2 The enlarged region of FTIR spectra of carbonyl groups in PDE-1, PDE-2, and PDE-3.

The compositions of PDE coatings were quantified. As reported previously [7, 8], normalization to the film thickness was first carried out on the FTIR spectra of the PDE, PEGDA, and PDMAEMA films. The peak area ratio of 1729 cm^{-1} ($A_{C=O}'$) to 2774 cm^{-1} ($A_{N\text{-}C\text{-}H}'$) in the PDMAEMA was calculated as X= $A_{C=O}'/ A_{N\text{-}C\text{-}H}'$. In the spectra of copolymer, the peak areas of the C=O stretching and N-C-H stretching were measured and denoted as $A_{C=O}$ and $A_{N\text{-}C\text{-}H}$. It is assumed that the absorption coefficient of each group is the same in the both homopolymer and copolymer. $A_{C=O(DMAEMA)}=X \bullet A_{N\text{-}C\text{-}H}$ can be used to calculate the peak area of C=O stretching from DMAEMA units in the copolymer. Therefore, the area of the C=O stretching from EGDA in the copolymer can be determined using: $A_{C=O(EGDA)}=A_{C=O}-X \bullet A_{N\text{-}C\text{-}H}$. The variation of the absorption

coefficient of the C=O stretching in DMAEMA and EGDA should be taken into consideration.

At the same coating thickness, by comparing the C=O stretching absorbance in the spectra of PDMAEMA ($A_{C=O(PDMAEMA)}$) and PEGDA ($A_{C=O(PEGDA)}$), the disparity can be observed. Under an assumption of equal density of the two homopolymers, the molar concentration ration of the C=O groups in PDMAEMA and PEGDA can be determined as $M_{EGDA}/2M_{DMAMEMA}$, where M_{EGDA} and M_{DMAEMA} are the molecular mass of EGDA and DMAEMA units, respectively. A factor of 2 represents two C=O groups in each EGDA unit. Therefore, the absorption coefficient ratio of C=O stretching absorbance from PDMAEMA and PEGDA (R) can be calculated and denoted as:

$$R = \frac{2A_{C=O(PDMAEMA)}M_{DMAEMA}}{A_{C=O(PEGDA)}M_{EGDA}} \quad (1)$$

According to the Beer-Lambert equation, the molar concentration and absorption coefficient of the corresponding unit are in proportion to the peak area of a specific vibration mode. Thus, equation (2) can be used to calculate the molar ratios of EGDA to DMAEMA in copolymers:

$$r = \frac{(A_{C=O} - X \bullet A_{N-C-H})R}{2X \bullet A_{N-C-H}} \quad (2)$$

Since there are two C=O groups in ach EGDA unit, a factor of 2 was introduced. Table 3.2 lists the calculated molar ratios.

Table 3.2 The molar ratio of EGDA to DMAEMA in copolymers.

Hydrogel	PDE-1	PDE-2	PDE-3
Feeding ratio (EGDA:DMAEMA)	1:3	1:5	1:10
Molar ratio (EGDA:DMAEMA) (r)	0.86	0.41	0.14

3.3.2 Short-term bacteria adhesion studies

Bacteria adhesion tests at different pH (pH 5, 6 and 7) were carried out on each copolymer surface. Figure 3.3 exhibits the bacteria adhesion on each coating relative to control after being subjected to bacteria suspension (10^7 cells/ml) over 1 hr Adhesion=$(N_{PDE}-N_{control})/N_{control}$ was used to calculate bacteria adhesion, where N_{PDE} and $N_{control}$ was the number of bacteria adhered to PDE coating and control surface.

It was obvious that PDE-3 was capable of adsorbing the highest amount of bacteria at all pH tested. The adhesion of PDE-3 was highest (1.5) at pH 5, due to the highest degree of ionization of DMAEMA components. As to PDE-2 coating, it was obvious that bacteria adhesion was the highest level at pH 5, and drastically decreased as the pH increased to pH 6. At pH 5 and 7, PDE-1 showed low bacteria adhesion compared with other hydrogel coatings. However, when it was immersed in the bacteria suspension at pH 6, the bacteria adhesion increased to 0.44, which showed an opposite trend to the other two polymer surfaces. Regardless of bacteria adhesion of PDE-1 at pH 6, the amount of adhering bacteria on the copolymers was in accordance with the assumption of more initial bacteria adhering on the surface with higher density of positive charges. The promotion of bacteria adhesion by positive charges was consistent with the observations in previous research [4, 5].

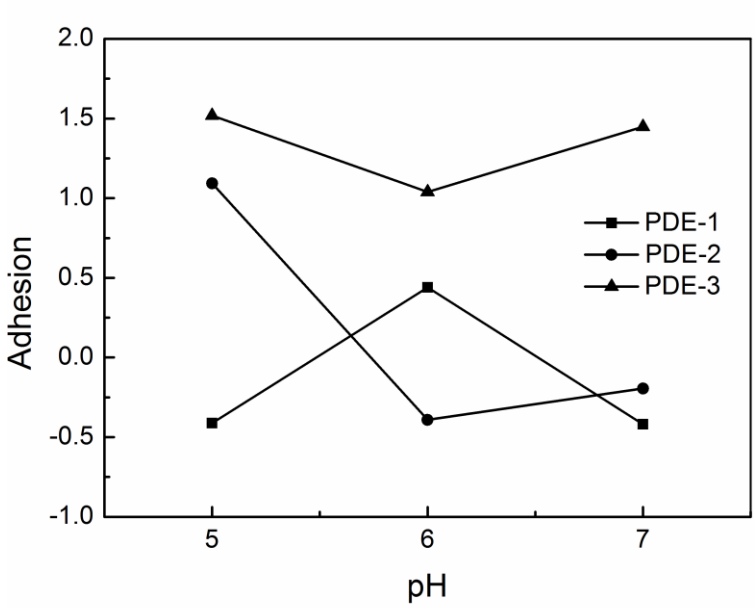

Figure 3.3 The bacteria adhesion at pH 5, 6 and 7 on the surfaces of PDE-1, PDE-2 and PDE-3 coatings.

3.3.3 Long-term bacteria viability studies

Long-term bacteria accumulation tests in ampicillin containing LB media were performed on the surfaces of PDE-1, PDE-2, PDE-3 and control plates after 1-hr incubation in *E. coli* solution (10^7 cells/ml) at different pH. Figure 3.4 exhibited the representative qualitative images of accumulated *E. coli* on the tested surfaces. On the uncoated control surfaces, the accumulations of biofilm at different pH were obvious and covered more than 50% of photographed areas. Compared the polymer coatings with control plate, less biofilm was observed on polymer coatings at pH 5, 6 and 7. The images exhibited that the biofilm formation on copolymers at different pH were of no significant difference. According to the 1-hr adhesion study, the bacteria adhesion on the PDE-3 coating was the highest. However, the lower level of further growth of bacteria

indicated an inhibition of bacteria growth on the positively charged surface. This is also consistent with the study in the chapter Ⅱ.

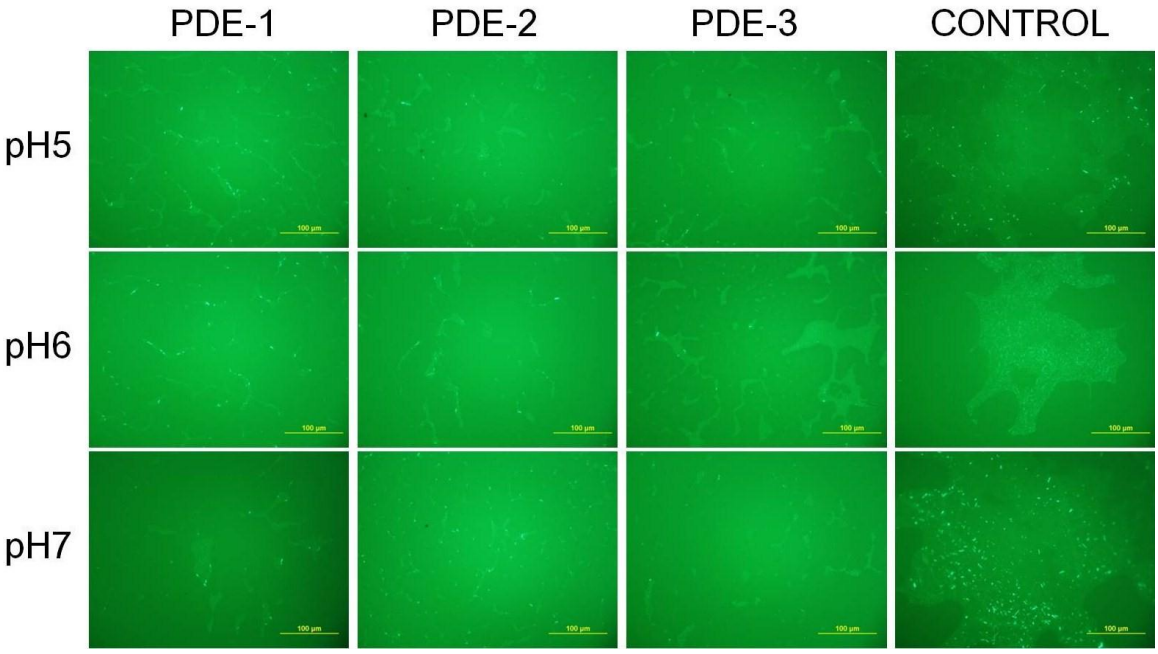

Figure 3.4 The images of the biofilm accumulation on each polymer coating at pH 5, 6 and 7.

Initial bacteria adhesion is considered as an essential factor causing the infection of implanted devices. However, the subsequent growth on the biomaterial surfaces has not been given much attention. In chapter Ⅱ, it was observed that bacteria adhesion was discouraged by negatively charged surfaces PME, while promoted by positively charged surfaces PDE. For the further growth, the strong electrostatic attraction of organisms inhibits the growth of Gram-negative bacteria on the positively charged surface.

3.4 Conclusion

Positively charged copolymer surfaces were designed with different densities of cationic moieties in order to investigate the antifouling effects on bacteria adhesion and accumulation. It was shown that the highest amount of initial bacteria adhering to the PDE-3 surface, which had the highest density of positive charge, while the PDE-3 inhibited further growth of bacteria. This study was consistent with the observation from previous test in chapter Ⅱ.

3.5 References

1. A.G. Gristina, *Science*, 1987, **237**, 1588.
2. B.A. Jucker, H. Harms and A. Zehnder, *Journal of bacteriology*, 1996, **178**, 5472-5479.
3. M. Van Loosdrecht, J. Lyklema, W. Norde and A. Zehnder, *Microbiology and Molecular Biology Reviews*, 1990, **54**, 75.
4. B. Gottenbos, D.W. Grijpma, H.C. Van Der Mei, J. Feijen and H.J. Busscher, *Journal of Antimicrobial Chemotherapy*, 2001, **48**, 7.
5. G. Harkes, J. Dankert and J. Feijen, *Journal of Biomaterials Science, Polymer Edition*, 1992, **3**, 403-418.
6. Y.M. Ye and Y. Mao, *Journal of Materials Chemistry*, 2011, **21**, 7946-7952.
7. K. Chan and K.K. Gleason, *Langmuir*, 2005, **21**, 8930-8939.
8. Y.M. Ye, Q. Song and Y. Mao, *Journal of Materials Chemistry*, 2011, **21**, 257-262
9. R. D. I. Scott, *The direct medical costs of healthcare-associated infections in U.S. hospitals and the benefits of prevention*, 2009.

CHAPTER IV

BIOMIMETIC GROWTH OF HYDROXYAPATITE ON ALIGNED POLYMER NANOTUBES

Abstract

Mineralization of hydroxyapatite (HA) on filamentous materials has been investigated for the development of scaffolds for bone tissue engineering to mimick the mineralized collagen fibrils in natural bone. However, fabrication of bone tissue engineering scaffolds with assembled, three-dimensional nanostructure reminiscent of mineralized collagen has been a challenge. We report a novel method in synthesizing mineralized polymer nanotubes with an aligned nanostructure. The aligned nanotubes have functional groups that promote apatite nucleation on the sidewalls, resulting in biomimetic growth of HA crystal and the formation of mineralized nanofibrils. The c-axis of the HA crystal was found to be parallel to the long axis of the polymer nanotube. The hybrid nanofibrils with preferentially oriented crystals resembling the natural bone structure are promising for applications in bone tissue engineering.

4.1 Introduction

Hydroxyapatite (HA) with the formula $Ca_{10}(PO_4)_6(OH)_2$ is a mineral form of calcium phosphate and a major component of natural bone, which consists of complex organizations with multiple levels of hierarchy [1, 2]. Based on the knowledge of bone structure, two factors are vital to activate effective bone regeneration [3]. One is the oriented apatite along the collagen fibrils [1, 3]. The other is the mimesis of three dimensional (3D) structures to fibril arrays of natural bone [1, 3]. Therefore, biomimetic mineralization, from the lowest level of hybrid HA/fibril composites to 3D structure of scaffolds, has been considerably investigated for bone regeneration in recent years.

To mimic mineralized fibrils, a variety of fibrous materials, including natural fibrils and synthetic macromolecules, has been studied on biomineralization. Fibrils from nature demonstrate superior capabilities of crystal induction. It was reported that oriented apatite crystal layers formed after 6-day mineralization of turkey tendon [4]. Similarly, type I collagen extracted from equine tendon was subjected to calcium ion containing solution to obtain mineralized collagen for the study of the role of collagen during apatite nucleation [5, 6]. Spider silk fibroin was also a candidate to induce the apatite nuclei that growing along a preferential orientation due to the favorable orientation of protein nanocrystals of silk [7]. In addition to natural materials, synthetic fibers exhibited mineralizable abilities as well. Mineralization of self-assembled peptide-amphiphile nanofibers was studied and the results showed oriented growth of apatite crystals [8]. Surface modified ethylene-vinyl alcohol copolymer (EVOH) fibers were subjected to simulated body fluid (SBF) incubation, and apatite deposited EVOH fibers were obtained

[9]. Although mineralized fibrils with oriented apatite were obtained, it was difficult to arrange these fibrils into 3D structure.

At the three dimensional level, mineralization of synthetic polymer scaffolds has been widely studied. Several techniques have been used to manufacture 3D polymeric scaffolds for biomimetic mineralization, including electrospinning [10, 11], solvent casting and salt leaching [12], gas foaming and particulate leaching [13], and thermally induced phase separation technique [14]. All these polymeric scaffolds exhibited the capability of mineralization. However, the structures of these polymer scaffolds were not similar to natural bone structure, which consisted of fibril arrays in regular pattern. Besides, oriented apatite crystals were not obtained on the surfaces of scaffolds.

The disadvantages of mineralized fibrils and scaffolds imply that they are not effective to activate the regenerative process. Therefore, a scaffold with the structure of regular fibril array with oriented growth of apatite is necessary. To fabricate such scaffold, templating of porous membrane combine with initiated chemical vapor deposition (iCVD) takes advantage due to the capability of obtaining conformal polymer coatings. As long as templates are fine enough, it is possible to synthesize polymeric scaffold with desired structure.

We hereby report the synthesis of 3D filamentous scaffold using iCVD. Biomineralization of these aligned polymer nanotubes were studied. Mineralized poly(methacrylic acid-*co*-ethylene glycol diacetate) (P(MAA-*co*-EGDA)) scaffold with aligned nanotubes were synthesized using supersaturated HA solutions and revised

simulated body fluid (rSBF). Morphologies and crystallinity of the apatite crystals were investigated.

4.2 Experimental

4.2.1 Materials and methods

Ethylene glycol diacetate (EGDA) (90%), methacrylic acid MAA (99%), and tert-butyl peroxide (TBP) (98%) were purchased from Sigma-Aldrich and were used as received. Silicon wafers were purchased from MEMC Electronic Materials and used as planar substrates during iCVD deposition. Polycarbonate (PC) membranes (Nuclepore) with pores of around 400 nm in radius and thickness of 10 μm were purchased from Fisher Scientific and used as the template for nanotubes fabrication. Hydroxyapatite (HA) was purchased from Sigma-Aldrich and used without further purification.

4.2.2 Synthesis of polymer nanotubes

The iCVD deposition was implemented in a custom built reactor (Sharon Vacuum) as previously reported [15, 16]. During deposition, the initiator was evaporated and fed at room temperature, while the EGDA and MAA monomers were heated up to 60 ℃ and 45 ℃, respectively. The vapors were pumped into the reactor through mass flow controllers (MKS Instruments, model 1479A and 1150) and mixed in the reactor. The flow rates of EGDA and MAA were 0.08 sccm and 0.24 sccm, respectively. The relative growth of polymer coatings was monitored on a reference Si wafer using in-situ interferometry. After iCVD coating on the PC membrane template, polymer nanotubes

were obtained by dissolving the template in chloroform. The schematics of polymer nanotube synthesis are shown in Figure 4.1.

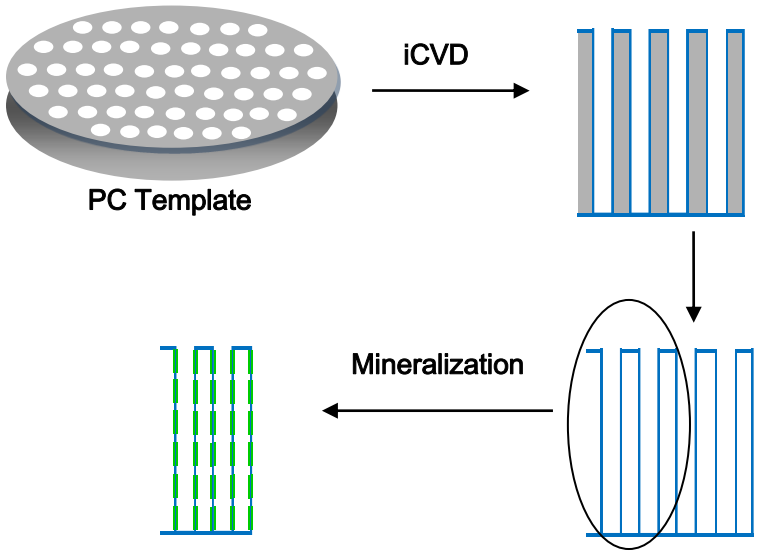

Figure 4.1 Schematics of the nanotube synthesis and the mineralization.

4.2.3 Biomimetic mineralization

Supersaturated HA solution ($[Ca^{2+}]$ = 4mM) was prepared following the reported protocol [17]. 2.5 g HA powder was dissolved in 250 mL 100 mM HCl solution, followed by the addition of deionized water to form 500 mL 50 mM stock solution with pH=2. Subsequently 0.2 mol NaCl was dissolved in 80 mL of 50 mM stock solution to increase the stability of HA solution. The pH value of the solution was adjusted to 7.0 using a 0.05 M KOH solution. Finally, the solution was made up to 1 L of HA solution using deionized water.

Revised simulated body fluid (rSBF) was prepared by subsequently adding 211.5 mM NaCl, 4.5 mM KCl, 1.5 mM K_2HPO_4, HCl (1 M), 3.75 mM $CaCl_2$ and 0.75 mM Na_2SO_4 into deionized water. The pH was adjusted to 6.4 using Tris. The ionic concentration and ionic strength of human body fluid, and Mg^{2+} and HCO^{3-} free rSBF are listed in the Table 4.1.

Table 4.1 Ionic concentration and ionic strength of human blood and rSBF

Ion conc. (mM)	Na^+	K^+	Ca^{2+}	Mg^{2+}	HCO_3^-	Cl^-	HPO_4^{2-}	SO_4^{2-}	Ionic strength
Blood plasma	142	5	2.5	1.5	27	103	1	0.5	149.5
rSBF	213	7.5	3.75	0	0	263	1.5	0.75	253.75

The polymer nanotubes were immersed in mineral solutions and incubated at 37 ℃ for different periods of time (1 week, 2 weeks and 3 weeks). The incubation solutions were refreshed every two days to keep calcium ions at same level. After being removed out of the solutions, polymer nanotubes were washed with deionized water for three times and dried overnight at room temperature.

4.2.4 Characterization

Fourier Transform Infrared (FTIR) was used to analyze the chemical structure of mineralized nanotubes collected on a silicon wafer. FTIR was conducted on a Nicolet 6700 spectrometer with DTGS detector under the transmission mode. For x-ray diffraction analysis (XRD), mineralized nanotubes were collected on a PMMA specimen holder and analyzed using a Bruker D8 Advance model (Bruker, U.S.). The operating

voltage and current were set at 40 kV and 40 mA, respectively. Morphologies of the mineralized nanotubes were observed using a FEI Quanta 600F scanning electron microscope (SEM) (FEI, Japan).

Transmission electron microscopy (TEM) and selected area electron diffraction (SAED) were carried out to study the orientation of HA crystals. The mineralized nanotubes were ultrasonically separated for 1 min. Afterwards the nanotube suspension was transferred to a copper grid for TEM. A JEOL JEM-2100 TEM was performed at 200kV. The elemental analysis was performed using the Evex Nanoanalysis energy dispersive x-ray spectroscopy (EDS).

4.3 Results

4.3.1 Synthesis of polymer nanotubes

Polycarbonate (PC) membranes with 400 nm pore size were used as a template to synthesize the P(MAA-*co*-EGDA) nanotubes. PC membranes were mounted on the glass slides and put in the reactor. The vapors of MAA and EGDA were delivered to the reactor to start the polymerization. Thin films were conformally deposited inside the PC membranes pores. P(MAA-*co*-EGDA) nanotubes were then obtained by dissolving the PC membrane in chloroform. Figure 4.2 shows the FTIR spectra of the PC template, a P(MAA-*co*-EGDA) coated template, the P(MAA-*co*-EGDA) nanotubes, and the corresponding P(MAA-*co*-EGDA) coating. In the spectrum of the coated template, the broad peak above 3000 cm^{-1} was attributed to the adsorption of –COOH groups in MAA,

while the adsorption from 1700 cm^{-1} to 1735 cm^{-1} was assigned to the stretching of C=O groups from both EGDA and MAA moieties.

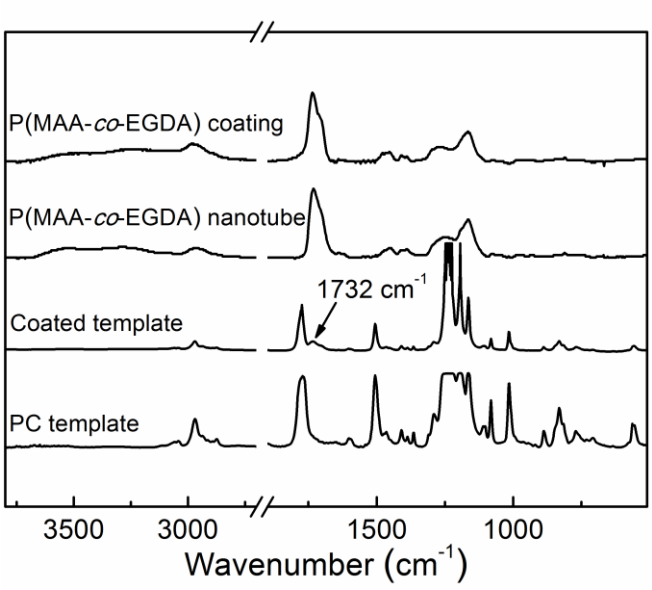

Figure 4.2 FTIR spectra of PC template, P(MAA-*co*-EGDA) coated template, P(MAA-*co*-EGDA) nanotubes, and P(MAA-*co*-EGDA) coating.

Four P(MAA-*co*-EGDA) copolymers with different compositions were synthesized and denoted by C1, C2, C3 and C4. The compositions of P(MAA-*co*-EGDA) copolymers (C1-C4) were quantified using FTIR analysis. Prior to the analysis, FTIR spectra of PMAA, PEGDA and P(MAA-*co*-EGDA) copolymer coatings were normalized to the coating thickness. The Peak Resolve tool in Omnic Software was used to decouple peaks, and subsequently the peak areas of the C=O stretching in MAA at 1702 cm^{-1} and in EGDA at 1735 cm^{-1} were measured. Based on the Beer-Lambert Law, at the same coating thickness, the absorbance peak area of C=O was proportional to the concentration of the unit and the corresponding absorption coefficient. According to previous work on

other acrylic copolymers [18], it is assumed that the absorption coefficients of the C=O adsorption are the same in the P(MAA-*co*-EGDA) copolymers as in PMAA and PEGDA homopolymers, respectively. The ratio of the EGDA mole concentration in P(MAA-*co*-EGDA) (C_{EGDA}) to the EGDA mole concentration in PEGDA (C^*_{EGDA}) can be calculated using: $C_{EGDA}/C^*_{EGDA}=A_{C=O(EGDA)}/A^*_{C=O(EGDA)}$, where $A_{C=O(EGDA)}$ and $A^*_{C=O(EGDA)}$ are the peak areas of the C=O absorption in the spectra of copolymer and homopolymer, respectively. Similarly, the ratio of the MAA mole concentration in copolymer (C_{MAA}) to the MAA mole concentration in PMAA (C^*_{MAA}) can be calculated as: $C_{MAA}/C^*_{MAA}=A_{C=O(MAA)}/A^*_{C=O(MAA)}$, where $A_{C=O(MAA)}$ and $A^*_{C=O(MAA)}$ are the peak areas of the C=O absorption in the spectra of copolymer and homopolymer, respectively. Putting two equations together, we can get:

$$\frac{C_{MAA}}{C_{EGDA}} = \frac{A_{C=O(MAA)}A^*_{C=O(EGDA)}C^*_{EGDA}}{A_{C=O(EGDA)}A^*_{C=O(MAA)}C^*_{MAA}}$$

Since mole concentration can be derived from the molecular mass and the density, C^*_{EGDA}/C^*_{MAA} is equal to M_{MAA}/M_{EGDA} under the assumption of equal density in PMAA and PEGDA coatings where M_{MAA} and M_{EGDA} are the molecular mass of the MAA and EGDA repeating units, respectively. The molar ratio of MAA units to EGDA units in each copolymer coating n_{MAA}/n_{EGDA} is equal to C_{MAA}/C_{EGDA} and can be calculated using the equation:

$$\frac{n_{MAA}}{n_{EGDA}} = \frac{A_{C=O(MAA)}A^*_{C=O(EGDA)}M_{EGDA}}{A_{C=O(EGDA)}A^*_{C=O(MAA)}M_{MAA}}$$

The crosslinking degree (CD%) was calculated as the mole fraction of crosslinked monomer units: $CD\%=2/(n_{MAA}/n_{EGDA}+2)\times 100\%$. There is a factor of 2 due to each

EGDA unit has two C=O double bounds. The calculated n_{MAA}/n_{EGDA} molar ratio of four P(MAA-*co*-EGDA) nanotubes was summarized in Table 4.2.

Table 4.2 The compositions and diameters of P(MAA-*co*-EGDA) tubes.

Copolymer	n_{MAA}/n_{EGDA}	Crosslinking degree (%)	Diameter of template pore (μm)
C1	2.32	46.3	1
C2	1.50	57.1	1
C3	0.88	69.4	1
C4	0.87	69.7	0.4

SEM image (Figure 4.3 left) shows the cross section of the C4 polymer nanotubes after dissolving the template. Regardless of the damage during sample preparation, it is noted that nanotubes were well-aligned and in good shape after being subjected to dissolving treatment and sample preparation for SEM. The lengths of nanotubes were 10 μm, which matched with the original pore depth indicating conformed coating across the pores; and mean radiuses were around 400 nm. TEM image was taken after nanotube isolation (Figure 4.3 right). The parallel dark lines were the walls of a nanotube and the wall thickness was uniform. It was obvious that both outer and inner surfaces of walls were smooth and clean. Templating PC membrane combined with CVD of the insoluble polymer P(MAA-*co*-EGDA) successfully fabricated nanotubes with ultrathin walls (~45 nm thickness).

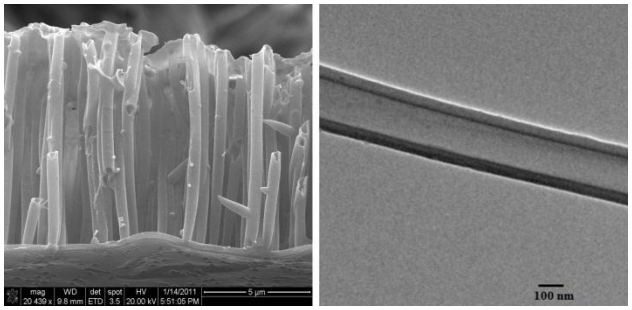

Figure 4.3 The SEM image of the synthesized P(MAA-*co*-EGDA) nanotubes (left) and the TEM image of a single polymer nanotube (right).

4.3.2 Formation of polymer nanotubes

Mechanical rigidity of polymer nanotubes, which is directly associated with crosslinking degree (CD%) of copolymers, is a concern for maintaining the proposed structure during the mineralization and cell culture process. Herein, four P(MAA-*co*-EGDA) tubes (C1-C4) with different diameter and CD% were subjected to mineralization for 3 weeks. After HA mineralization, morphologies of the four tubes were shown in Figure 4.4. It was obvious that C1 tubes with the CD% of 46.3 completely collapsed and lost their tubular structures. They folded layer by layer like soft thin films. With the CD% of 57.1, C2 tubes collapsed as well, but their original tubular shape still could be distinguished individually. Increasing CD% to 69.4, C3 tubes maintained original tubular structure. At the same CD% but with the nanotube diameter of 400 nm, C4 nanotubes exhibited high mechanical rigidity and precise nanostructure. Therefore, in the following experiments, C4 nanotubes were chosen as the substrate for following study.

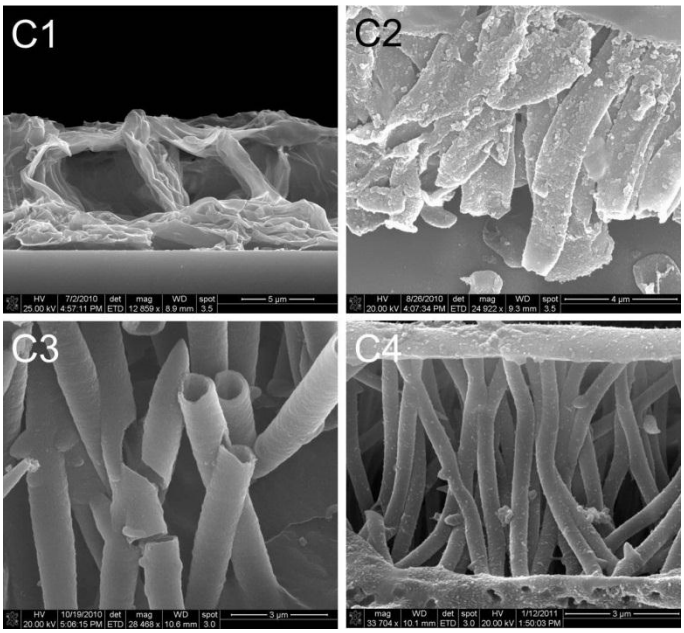

Figure 4.4 The cross section view of mineralized C1, C2, C3, and C4 tubes.

4.3.3 Mineralization of polymer nanotubes

4.3.3.1 Supersaturated HA solution

During the HA mineralization process, initial evidence of nuclei induction and crystal formation on the nanotubes was obtained using FTIR (Figure 4.5). New peaks appeared as incubation time prolonged. In the spectrum of 2-week incubated nanotubes, strong P-O peaks at: 1111cm^{-1} and 1025 cm^{-1} were attributed to the υ_3 mode of P-O; a peak at 960 cm^{-1} was assigned to the υ_1 P-O stretching mode; and the peaks at 560 cm^{-1} and 600 cm^{-1} were assigned to the υ_4 mode of P-O. In addition, a sharp peak at 3567cm^{-1} was attributed to the O-H stretching mode in HA [19]. These new peaks suggested the formation of hydroxyapatite on the surface of nanotubes after 2-week mineralization. In addition, the peaks at 560 cm^{-1} and 600 cm^{-1} indicated that apatite may be crystalline. As

to the nanotubes incubated for one week, although no obvious peaks ranging from 900 cm^{-1} to 1100 cm^{-1} appeared, there were two small peaks at 550 cm^{-1} and 601 cm^{-1} indicating the beginning of crystal formation. Significant new peaks at 1557 cm^{-1}, which may be attributed to ionization of –COOH into $–COO^-$ or combination of $–COO^-$ and Ca^{2+} [20], showed up in both spectra, while broad peaks from hydrogen bonds between –COOH groups in MAA units ranging from 3000 cm^{-1} to 3400 cm^{-1} were absent in both spectra. This suggested that calcium ions induction was achieved by ionization of the carboxyl groups.

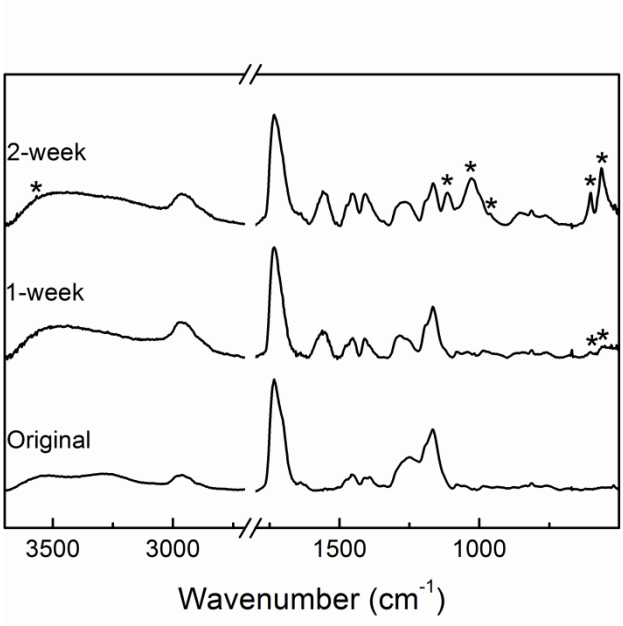

Figure 4.5 FTIR spectra of C4 nanotubes incubated in supersaturated HA solution at different period of time. Peaks of apatite are denoted by *.

XRD was taken on 2-week incubated nanotubes (Figure 4.6). Intense characteristic diffraction peaks of crystalline apatite were detected at 26 º, 31.7 º, 32.2 º and 53.5 º (2θ)

corresponding to (002), (211), (112) and (004) planes of apatite. The XRD results further verify that crystalline apatite formed on the polymer nanotubes.

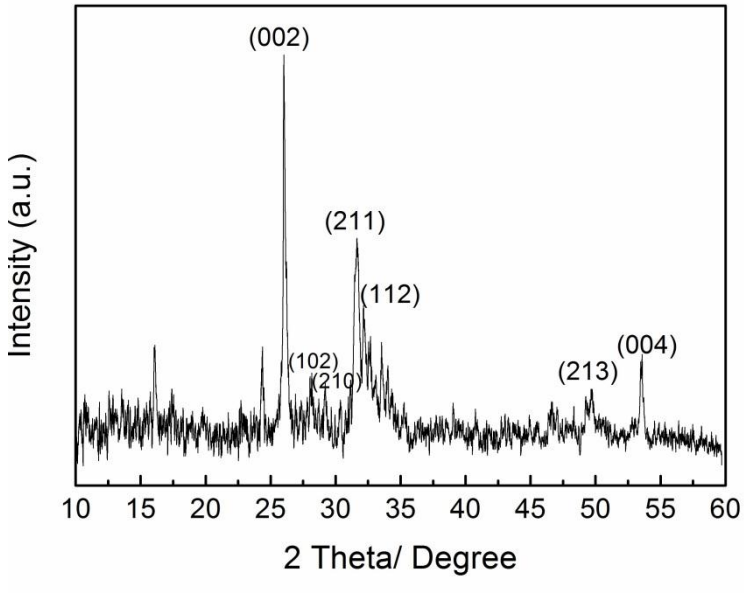

Figure 4.6 XRD spectrum of mineralized C4 nanotubes after 2-week incubation.

SEM images illustrate the change of outer wall morphologies of nanotubes during apatite growth. Before incubation, outer walls of nanotubes were smooth (Figure 4.7A). After 1-week incubation, the roughness increased, which indicated crystal growth on the surface (Figure 4.7B). Figure 4.7C shows more obvious film-like crystals homogeneously covering the entire surfaces of nanotubes after 2-week incubation.

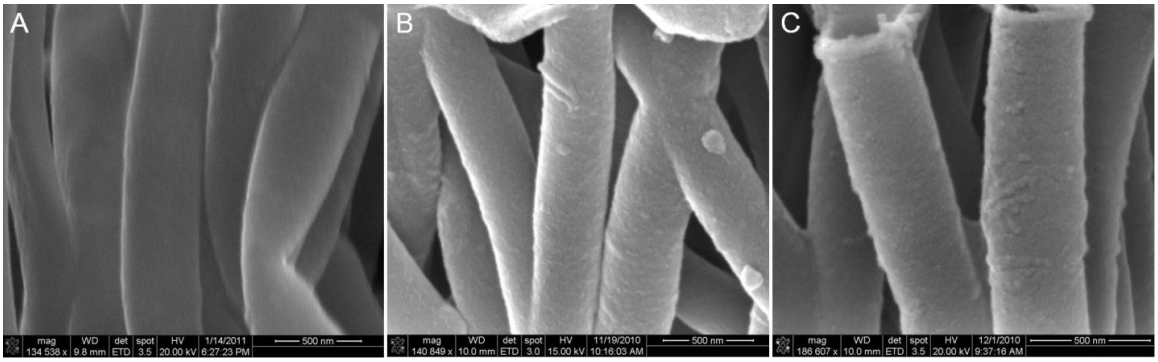

Figure 4.7 SEM images of C4 nanotubes A) before incubation, B) after 1-week incubation, C) after 2-week incubation in supersaturated HA solution.

Selected area electron diffraction (SAED) of the sample incubated two weeks was conducted to analyze the crystal orientation on the polymer nanotubes. Figure 4.8A shows the TEM micrograph of a section of a nanotube incubated two weeks. Compared with the SEM image (Figure 4.7C), fewer crystals remained on the nanotube surface, possibly due to the fact that crystals shed off from the surface during the ultrasonic preparation. There were still thin crystal layers left. SAED pattern of spots (Figure 4.8B) suggests the covering apatite was crystalline, which was consistent with the XRD and FTIR results. The presence of diffraction spots assigned to (002) and (004) planes, were detected. Surprisingly, the SAED patterns of apatite were spots, which was the characteristic pattern of monocrystalline apatite. This observation suggested preferential orientation of crystals on the nanotubes. In addition, the regular pattern revealed a single crystal which is consistent with results reported by other researchers [21, 22]. In Fig 4.8B, direction of double-headed arrow in (002) diffraction pattern indicated c axis direction of apatite crystal, which was parallel to the long axis of the nanotube. To examine crystal orientation, the SAED of the crystal was also taken by tilting it at an angle of 30 ° along

the direction perpendicular to the c axis. The preferential orientation of apatite with c axis parallel to long axis was stressed by the absence of spots indicating (002) and (004) planes and the presence of the spots from (102) plane (Figure 4.8C).

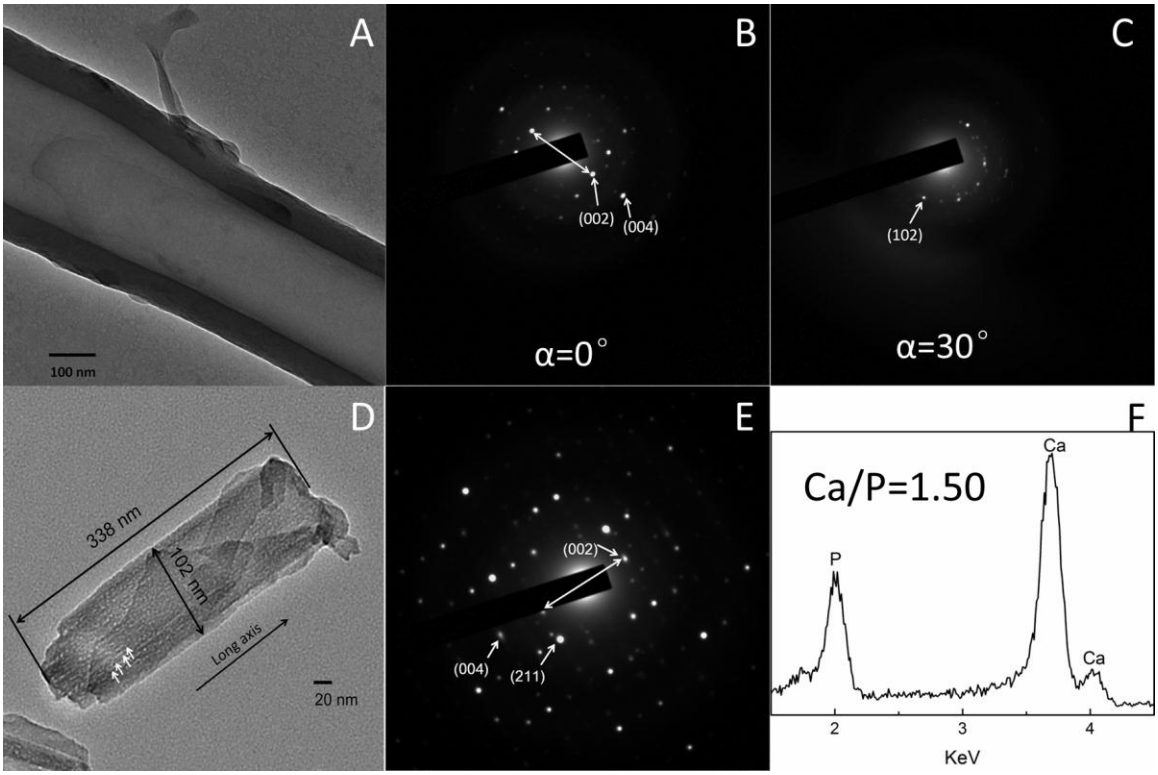

Figure 4.8 (A) The TEM micrograph of a C4 nanotube incubated in HA solution 2 weeks. (B) SAED pattern of the C4 nanotubes in A. (C) SEAD pattern of the same nanotube with a tilting angle of 30 °. (D) The TEM micrograph of an apatite crystal shed off from the C4 nanotubes. (D) SAED pattern of the apatite. (F) EDS spectra of the mineralized C4 nanotubes.

Since the loss of some crystals occurred during ultrasonic separation, the pieces of shed off crystals were also investigated. The TEM image is shown in the Figure 4.8D. The length of the piece was 338 nm and the width was 102 nm. Since the average of nanotube radius was measured 317±54nm and an arc-shape presented at the right end of the crystal piece, it was determined that the crystal shed off from one of nanotubes and

the long axis of the small piece was parallel to the length direction and the long axis of nanotubes. SAED pattern of the crystal piece exhibited the crystallinity, and the spots corresponded to (002), (004) and (211) planes. Similarly, the double-headed arrow on the Figure 4.8E revealed the c axis, which was parallel to the long axis of the crystal and nanotubes. In addition, white arrows in TEM image (Fig 4.8D) exhibited parallel crystal plates. Energy dispersive X-ray spectroscopy (EDS) (Figure 4.8F) reveals Ca/P ratio of 1.50, which was similar to Ca/P ratio in natural bone [23, 24].

4.3.3.2 Revised SBF (rSBF)

Similarly, the C4 nanotubes were also incubated in revised SBF (rSBF) solutions to process biomineralization. From FTIR spectra, it was noted that there was continuous growth of apatite on the surface of nanotubes (Figure 4.9). After 1-week incubation, although no obvious P-O absorption peaks were shown in the spectrum, a peak at 1557 cm^{-1} indicating the interaction between $–COO^-$ and Ca^{2+} was present [20]. The absence of peaks ranging from 3400 cm^{-1} to 3000 cm^{-1} was also consistent with COOH ionization. Induction of calcium ions by $–COO^-$ occurred as long as the samples were immersed in the solutions. After two-week incubation, a weak peak centering at 1109 cm^{-1} was attributed to the υ_3 mode of P-O. A sharp small peak at 3568 cm^{-1} was from the O-H stretching mode of HA. After three-week incubation, peaks from the υ_3 mode of P-O at 1108 cm^{-1} and 1037 cm^{-1}, and the υ_4 mode of P-O at 550 cm^{-1} were observed.

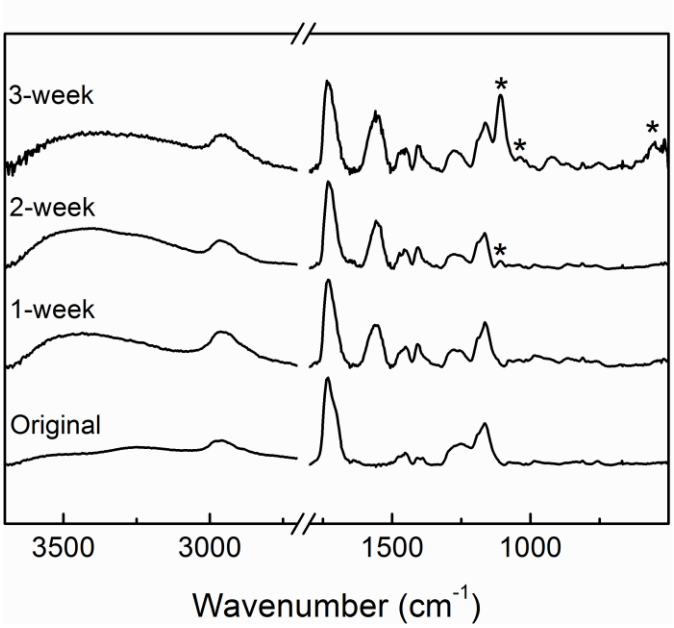

Figure 4.9 FTIR spectra of C4 nanotubes incubated in rSBF solution at different period of time. Peaks of apatite are denoted by *.

It was obvious that the amount of crystals was accumulated as incubation time extended (Figure 4.10). After 1-week incubation, topographies of nanotube surfaces were still as smooth as untreated tubes, while the roughness increased after 2-week incubation. Through 3-week incubation, a large amount of globule-like crystals growing on the surface was observed, which corresponded to the significant peak in FTIR spectrum.

Isolated nanotubes were observed under TEM to study their crystallinity as well. The nanotubes incubated 3 weeks were selected. From Figure 4.11A, it was evident that there were a large amount of crystals growing on the internal wall of the nanotube, while it was hardly observed crystals on the outer wall, which was covered by many globule-like crystals from SEM observation before ultrasonic treatment. This implied that the violent ultrasonic isolation caused the loss of apatite crystal. The SAED pattern (Figure

4.11B) of the sample showed that the crystals on the surface were apatite, and diffraction spots corresponded to the (002), (004) and (211) planes.

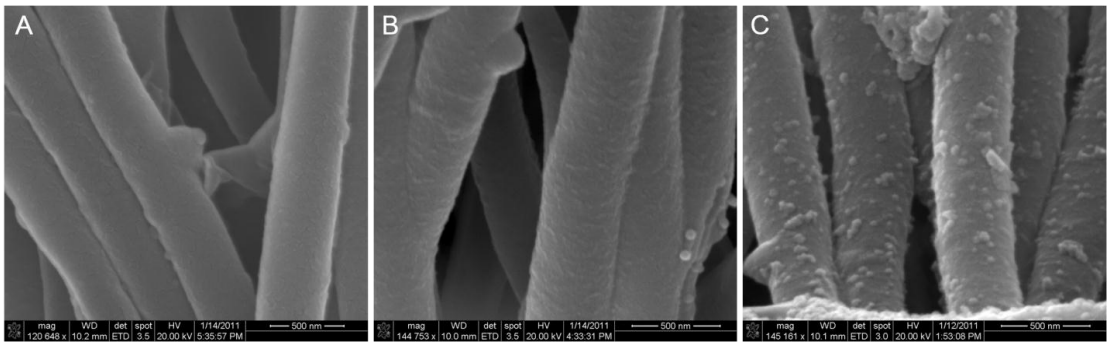

Figure 4.10 SEM images of mineralized C4 nanotubes A) after 1-week incubation, B) 2-week incubation, and C) 3-week incubation in rSBF solution.

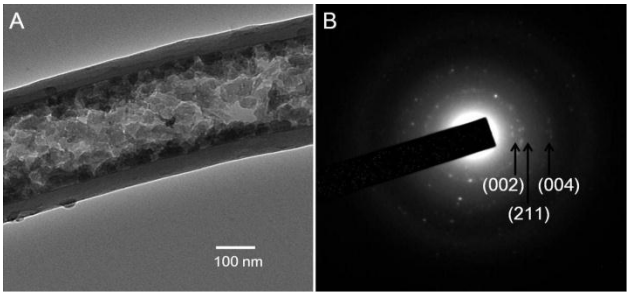

Figure 4.11 (A) The TEM micrograph of C4 nanotubes incubated in rSBF solution 3 weeks. (B) SAED pattern of selected area of the same polymer nanotubes.

4.4 Discussion

4.4.1 Mineralization from supersaturated HA solution

Surfaces containing negatively charged groups, such as $–HPO_4$ and –COOH groups, promote nucleation by establishing local ion supersaturation [25, 26]. In this study, copolymer P(MAA-*co*-EGDA) can induce the apatite nuclei, because it contains carboxyl

groups (-COOH), which can ionize into carboxylate ($-COO^-$). The mineralized nanotubes confirmed that the –COOH containing surfaces were capable of nucleating hydroxyapatite. The surprising detection was the preferential orientation of apatite crystals from supersaturated HA solution. The c-axis of apatite crystal is co-aligned with the long axis of polymer nanotubes. Therefore, formation of crystals was not random, but controlled and oriented. Although exact control mechanisms are not clearly known, formation of oriented apatite crystals have been conducted and reported on natural collagen fibers [1, 4, 3], silk fibroin [7], synthetic polymer fibers [8, 27] and bacteriophage fibrils [28], which are of densely packed structure and specifically arranged functional groups. The orientation control may be achieved by specific stereochemical arrangement of acidic groups that promote nucleation of apatite in a particular way driven by an epitaxial mechanism [25, 29, 30].

Synthetic polymer fibrils are promising for biomimetic mineralization study. Although oriented nuclei have been obtained by using assembled peptide-amphiphile nanofibers, two dimensional (2D) nanofibers did not fulfill the 3D structure requirement for bone regeneration [8]. So far, a great number of efforts have been made on fabrication of a 3D polymer matrix and a variety of techniques have been applied. To the best of our knowledge, mineralization of 3D polymeric scaffolds has not achieved oriented apatite on their surfaces. In this study, the 3D aligned nanotubes were fabricated using iCVD. Since the c axis of apatite is parallel to the long axis of collagen in natural bone, mineralized nanotubes obtained in this study are promising for bone tissue engineering. Furthermore, the structure of the pre-aligned nanotubes resembles parallel fibril array in natural bone. Therefore, they may be able to activate the regenerative process.

4.4.2 Influence of rSBF on crystal growth

More factors influence the nucleation of apatite from SBF than supersaturated HA solution. Since Mg^{2+} and HCO_3^- have been reported as inhibitors of crystal growth [31], in this study rSBF was prepared without these two ions.

From the FTIR spectra (Figure 4.5 and Figure 4.9), the speed of crystal growth was slower in rSBF than HA solution. One possible reason is a higher concentration of Ca^{2+} (4 mM) in HA solution. The other reason may be higher ionic strength of rSBF (Table 4.1), which makes the Ca-P solution stable and delays the precipitation of Ca-P in solution [32]. In other words, Na^+ contributes to high ionic strength and keeps supersaturation of Ca^{2+} in the solution, which allows Ca-P to nucleate on the substrate surface over a relatively longer time. Compared with the morphology of crystals obtained from HA solution (Figure 4.7C and Fig 4.10A), more globule crystals on the inner wall and outer wall may be attributed to more nuclei from rSBF due to its higher ionic strength. As to crystal orientation, it was random and crystals were polycrystalline rather than monocrystalline. There are more components in rSBF, such as SO_4^{2-} and K^+, can disturb crystal lattice formation. Further study is needed on influence of each component on crystal structure.

4.5 Conclusion

In this study, aligned P(MAA-*co*-EGDA) nanotubes with 3D structure were fabricated using iCVD followed by dissolving of the template. Mineralized nanotubes were obtained by incubating in supersaturated HA solution and rSBF. Apatite crystals

from HA solution were monocrystalline and had oriented growth. C-axes of crystals were parallel to long axes of nanotubes. Crystals with Ca/P ratio of 1.5 are similar to natural bone. Since there are more factors influencing the crystal structure using rSBF, the crystals were polycrystalline and had no preferential orientation.

4.6 References

1. S. Weiner and H.D. Wagner, *Annual Review of Materials Science*, 1998, **28**, 271-298.
2. W. Traub, T. Arad and S. Weiner, *Proceedings of the National Academy of Sciences of the United States of America*, 1989, **86**, 9822-9826.
3. A. Tampieri, S. Sprio, M. Sandri and F. Valentini, *Trends in Biotechnology*, 2011, **29**, 526-535.
4. S.S. Jee, R.K. Kasinath, E. DiMasi, Y.Y. Kim and L. Gower, *Crystengcomm*, 2011, **13**, 2077-2083.
5. N. Roveri, G. Falini, M.C. Sidoti, A. Tampieri, E. Landi, M. Sandri and B. Parma, *Materials Science & Engineering C-Biomimetic and Supramolecular Systems*, 2003, **23**, 441-446.
6. F. Nudelman, K. Pieterse, A. George, P.H.H. Bomans, H. Friedrich, L.J. Brylka, P.A.J. Hilbers, G. de With and N. Sommerdijk, *Nature Materials*, 2010, **9**, 1004-1009.
7. B. Cao and C. Mao, *Langmuir*, 2007, **23**, 10701-10705.
8. J.D. Hartgerink, E. Beniash and S.I. Stupp, *Science*, 2001, **294**, 1684-1688.
9. Y. Yokoyama, A. Oyane and A. Ito, *Journal of Biomedical Materials Research Part B: Applied Biomaterials*, 2008, **86**, 341-352.
10. P.A. Madurantakam, I.A. Rodriguez, C.P. Cost, R. Viswanathan, D.G. Simpson, M.J. Beckman, P.C. Moon and G.L. Bowlin, *Biomaterials*, 2009, **30**, 5456-5464.
11. F. Yang, J.G.C. Wolke and J.A. Jansen, *Chemical Engineering Journal*, 2008, **137**, 154-161.
12. A.C. Jayasuriya, C. Shah, N.A. Ebraheim and A.H. Jayatissa, *Biomedical Materials*, 2008, **3**.
13. S.S. Kim, M.S. Park, S.J. Gwak, C.Y. Choi and B.S. Kim, *Tissue Engineering*, 2006, **12**, 2997-3006.
14. X. Liu, L.A. Smith, J. Hu and P.X. Ma, *Biomaterials*, 2009, **30**, 2252-2258.
15. Y.M. Ye, Q. Song and Y. Mao, *Journal of Materials Chemistry*, 2011, **21**, 257-262.
16. Y.M. Ye and Y. Mao, *Journal of Materials Chemistry*, 2011, **21**, 7946-7952.
17. C.B. Mao, H.D. Li, F.H. Cui, C.L. Ma and Q.L. Feng, *Journal of Crystal Growth*, 1999, **206**, 308-321.
18. K. Chan and K.K. Gleason, *Langmuir*, 2005, **21**, 8930-8939.

19. A. Antonakos, E. Liarokapis and T. Leventouri, *Biomaterials*, 2007, **28**, 3043-3054.
20. S. Sindhu and S. Valiyaveettil, *Journal of Polymer Science Part B-Polymer Physics*, 2004, **42**, 4459-4465.
21. M. Espanol, J. Portillo, J.M. Manero and M.P. Ginebra, *Crystengcomm*, 2010, **12**, 3318-3326.
22. G. Ma and X.Y. Liu, *Crystal Growth and Design*, 2009, **9**, 2991-2994.
23. D.M. Liu, T. Troczynski and W.J. Tseng, *Biomaterials*, 2001, **22**, 1721-1730.
24. M.P. Ginebra, E. Fernández, F. Driessens and J.A. Planell, *Journal of the American Ceramic Society*, 1999, **82**, 2808-2812.
25. S. Weiner and L. Addadi, *Journal of Materials Chemistry*, 1997, **7**, 689-702.
26. Q. Liu, J. Ding, F.K. Mante, S.L. Wunder and G.R. Baran, *Biomaterials*, 2002, **23**, 3103-3111.
27. S. Yang, H. He, L. Wang, X.R. Jia and H.L. Feng, *Chemical Communications*, 2011, **47**, 10100-10102.
28. F.K. Wang, B.R. Cao and C.B. Mao, *Chemistry of Materials*, 2010, **22**, 3630-3636.
29. J. Aizenberg, A.J. Black and G.M. Whitesides, *Nature*, 1999, **398**, 495-498.
30. S. Mann, J.P. Hannington and R.J.P. Williams, *Nature*, 1986, **324**, 565-567.
31. F. Barrere, P. Layrolle, C. Van Blitterswijk and K. De Groot, *Bone*, 1999, **25**, 107S-111S.
32. F. Barrere, C. Van Blitterswijk, K. De Groot and P. Layrolle, *Biomaterials*, 2002, **23**, 1921-1930.

CHAPTER V

CONCLUSION AND SUGGESTIONS

5.1 Conclusion

In this thesis, novel polymeric biomaterials have been developed for antifouling application and bone tissue engineering, and their properties were verified. In order to study individual applications, two kinds of polymers were synthesized. For nonfouling surfaces, ampholytic polymer poly(methacrylic acid-*co*-2-dimethylamino ethyl methacrylate-*co*-ethylene glycol diacrylate) (PMDE) with both cationic and anionic moieties was synthesized. Bacteria resistance was achieved at pH 5, 6 and 7. Besides, the influence of positive charges on nonfouling properties was studied. For resemblance of bone tissue, copolymer poly(methacrylic acid-*co*-ethylene glycol diacrylate) (P(MAA-*co*-EGDA)) was deposited on a porous template to fabricate aligned nanotubes. Their capabilities of apatite induction have been verified. Both materials were synthesized through initiated chemical vapor deposition (iCVD), which provides an ideal methodology for fabrication of conformal coatings on nanoscaled substrates.

5.1.1 Nonfouling coatings of PMDE

Polyampholytes of PMDE, containing unequal amounts of cationic 2-dimethylamino ethyl methacrylate (DMAEMA) and anionic methacrylic acid (MAA) monomers, were synthesized via iCVD. From the swelling tests, isoelectric points (pI) of the synthesized polyampholytes were at around pH 5. Polyampholytes were subjected to the bacteria adhesion and accumulation tests for 1 hr and 24 hr. In the 1-hr bacteria adhesion study, more than 99% of bacteria were reduced on the polyampholyte coatings at pH 7; while no biofilm was observed in the 24-hr accumulation study. The influence of pH on the nonfouling properties was also investigated. Synthesized polyampholyte

coatings effectively discouraged both bacteria adhesion and biofilm accumulation at pH 5, 6 and 7.

5.1.2 Antifouling effects of positively charged surfaces

Poly(2-dimethylamino ethyl methacrylate-*co*-ethylene glycol diacrylate) (PDE) coatings with different densities of cationic units were used to investigate antifouling effects of positive charges on bacteria adhesion and accumulation. It is proven that the higher the density of positive charge was on the surface, the more bacteria adhered in the 1-hr bacteria adhesion study. In addition, positively charged surface inhibited biofilm formation in the 24-hr bacteria accumulation study.

5.1.3 Biomimetic mineralization of aligned nanotubes

Three dimensional (3D) structure nanotubes were successfully fabricated through vapor based deposition. These nanotubes were composed of ethylene glycol diacrylate (EGDA) and methacrylic acid (MAA), which was effective to induce apatite nuclei. After being incubated in supersaturated hydroxyapatite (HA) solution and revised simulated body fluid (rSBF) for a certain period of time (1 week, 2 weeks and 3 weeks), mineralized nanotubes were obtained. C-axis of the mineralized apatite from HA solution was parallel to long axis of the nanotube, while polycrystalline apatite crystals were obtained from rSBF.

5.2 Suggestions for future study

In this thesis, a new avenue has been opened for development of novel polymeric biomaterials for biomedical uses. Novel polyampholytic polymers and aligned nanotubes

have achieved bacteria resistance and mineralization, respectively. However, from a scientific perspective, improvement and further study should be implemented to verify their properties for in vivo applications.

First, nonfouling capability can be influenced by a variety of chemical and structural factors, including thickness of film [1], electric neutrality on the surface [2] and surface wettability [3]. The examination of influence of thickness on nonfouling properties of polyampholytes should be further conducted. In addition, the chemical structures of ampholytic polymers are still unknown due to the similarity of monomers in the backbone. If the structure can be detected, it is easy to extrapolate the mechanism of the vapor-based polymerization of oppositely charged moieties. Moreover, the cytotoxicity of the polyampholytes should be investigated.

Second, as to bone regeneration, a study is needed to verify the relationship between apatite orientation and chemical structure of polymer. The relationship can direct and make mimesis of bone tissue more conveniently via vapor-based deposition as long as a fine template available. The effect of polymer on growth of osteoblast should be taken into consideration as well.

Third, it is worth mentioning the multifunctional properties of synthesized polymers in this thesis. One possibility is that polyampholytes may be used to fabricate nanotubes for mineralization as well. It is reported that both -COOH and $–NH_2$ groups are capable of inducing nuclei [4]. Since cationic and anionic monomers interact during deposition, they may form an oriented arrangement of these groups. Also, it is more similar to the amino acid which is the component of collagen. Hence, formation of

oriented growth of apatite crystal may be controllable and accelerated. This can be a direction for further study. Besides, according to previous study, antibacterial coatings of fluoridated hydroxyapatite were obtained for percutaneous implants [5]. Therefore, the mineralized nanotubes can also be utilized as antimicrobial materials. Further investigation of mineralized polymers can be conducted on antimicrobial properties.

5.3 References

1. C. Zhao, L. Li, Q. Wang, Q. Yu and J. Zheng, *Langmuir*, 2011.
2. E. Ostuni, R.G. Chapman, R.E. Holmlin, S. Takayama and G.M. Whitesides, *Langmuir*, 2001, **17**, 5605-5620.
3. G.B. Sigal, M. Mrksich and G.M. Whitesides, *Journal of the American Chemical Society*, 1998, **120**, 3464-3473.
4. I. Hirata, M. Akamatsu, E. Fujii, S. Poolthong and M. Okazaki, *Dental materials journal*, 2010, 1007160044.
5. X. Ge, Y. Leng, C. Bao, S.L. Xu, R. Wang and F. Ren, *Journal of Biomedical Materials Research Part A*, 2010, **95**, 588-599.

VITA

TONG LIU

Candidate for the Degree of

Master of Science

Thesis: SYNTHESIS AND BIOMEDICAL APPLICATIONS OF POLYMER NANOMATERIALS

Major Field: Biosystems Engineering

Biographical:

Education:

Completed the requirements for the Master of Science in Biosystems Engineering at Oklahoma State University, Stillwater, Oklahoma in December, 2011.

Completed the requirements for the Bachelor of Science in Environmental Engineering at China University of Mining and Technology (Beijing), Beijing, China in 2009.

Experience:
Worked as a graduate assistant at Oklahoma State University from 2010-2011.
Worked as a research assistant at Tsinghua University and China University of Mining and Technology (Beijing) from 2008-2009.

Name: TONG LIU Date of Degree: May, 2012

Institution: Oklahoma State University Location: Stillwater, Oklahoma

Title of Study: SYNTHESIS AND BIOMEDICAL APPLICATIONS OF POLYMER NANOMATERIALS

Pages in Study: 73 Candidate for the Degree of Master of Science

Major Field: Biosystems Engineering

Scope and Method of Study:
Polymeric materials have been vitally important in biomedical applications. To enhance the biocompatibility of implanted devices and to activate the process of bone tissue regeneration, surface modification and scaffold fabrication are employed, respectively. Polymeric nanomaterials with biofunctional groups can fulfill these purposes. Initiated chemical vapor deposition (iCVD) with the advantages of conformality and solvent-free process was used to synthesize polymer coatings for nonfouling applications and scaffolds for bone tissue engineering.

Findings and Conclusions:
Using iCVD technique, surface modification and fabrication of a three-dimensional scaffold were successfully achieved. In CHAPTER Ⅱ, novel polyampholytic coatings for nonfouling applications were reported. More than 99% of bacteria were resisted by hydrogel coatings in bacteria adhesion tests, and no biofilm formed on the surfaces after 24-hr incubation. In CHAPTER Ⅲ, antifouling effects of positively charged surfaces were investigated. It was demonstrated that positively charged surfaces promoted bacteria adhesion in short term but inhibited bacteria growth to form the biofilm. In CHAPTER Ⅳ, a polymeric scaffolds consisting of aligned structure and oriented apatite growth were fabricated. Biomimetic mineralization of nanotubes was achieved. The crystal from supersaturated HA solution was preferentially oriented with the c-axis parallel to the long axis of nanotubes.

ADVISER'S APPROVAL: Dr. Yu Mao